A multi-indicator framework for assessing the likelihood of ENSO impacts across southern Africa

Authors:

Tamuka Magadzire*[1,2], Surekha Ramessur[3], Sunshine Mduduzi Gamedze[3], Nicholas Christopher Mbangiwa[2], Kgakgamatso Mphale[2], Gregory Husak[1], Laura Harrison[1], Chris Funk[1]

[1] University of California, Santa Barbara Climate Hazards Center, Santa Barbara, USA

[2] Department of Physics, School of Physical and Life Sciences, University of Botswana, Gaborone, Botswana

[3] Southern African Development Community Climate Services Centre, Gaborone, Botswana

∗ Corresponding author email: magadziret@ub.ac.bw

Peer Review Status:

This is a non-peer-reviewed preprint submitted to EarthArXiv

A multi-indicator framework for assessing the likelihood of ENSO impacts across southern Africa

Tamuka Magadzire*[1,2], Surekha Ramessur[3], Sunshine Mduduzi Gamedze[3], Nicholas Christopher Mbangiwa[2], Kgakgamatso Mphale[2], Gregory Husak[1], Laura Harrison[1], Chris Funk[1]

[1] University of California, Santa Barbara Climate Hazards Center, Santa Barbara, USA

[2] Department of Physics, School of Physical and Life Sciences, University of Botswana, Gaborone, Botswana

[3] Southern African Development Community Climate Services Centre, Gaborone, Botswana

∗ Corresponding author email: magadziret@ub.ac.bw

Abstract

The El Niño-Southern Oscillation (ENSO) is the dominant source of seasonal predictability for Southern Africa, yet operational guidance rarely conveys which agriculturally relevant variables it can skillfully predict, or where ENSO impacts are most likely. We present an operational analysis framework that converts an ENSO state, classified by phase and strength, into gridded, analogue-composite outlooks for 14 indicators spanning rainfall, evaporative demand and related standardized indices (SPI and SPEI), crop water balance, dry-spells, rainfall-season timing, and heat extremes. El Niño typically produces the adverse outcome across the central and southern interior, with Moderate-to-Strong events having more robust impacts. We assess skill with cross-validated ranked probability skill scores at the grid-cell scale and aggregated over the response domain, and phase-specific verification scores. Predictability is substantial but uneven: temperature and potential evapotranspiration are the most predictable. Rainfall is skillful across much of the core though spatially variable. Crop water balance, season length and a smoothed dry-spell metric are skillful as regional indices, while the onset and cessation dates carry little skill. Skill peaks at the height of the rains, is weaker for La Niña than El Niño, and increases with event strength. A single ENSO-based outlook can be misleading. Outlook guidance, including confidence should be set by location, season, indicator, phase and event strength, with strong or very strong El Niño events being most impactful. This is relevant to the very strong El Niño forecast for 2026/27. The framework is delivered openly through the Southern Africa ENSO Explorer (https://enso.ubramplab.org).

1. Introduction

The El Niño-Southern Oscillation (ENSO) is the dominant source of seasonal predictability for southern Africa: El Niño tilts the region toward drier, hotter growing-season conditions and La Niña toward wetter ones (Ropelewski & Halpert, 1987) and has been shown to shift rainfall probabilities more strongly under stronger events (Pomposi et al., 2018). The 2015/16 El Niño produced the region's most severe drought in decades, and the 2023/24 El Niño again drove

widespread crop failure and food insecurity across the maize-dependent interior, while the strong 1997/98 El Niño produced a more muted impact than anticipated. These variations underscore the need to understand the probabilities, risks and uncertainties associated with ENSO's influence across a range of indicators with a direct bearing on societal impacts like agriculture, water resources and health. This need is particularly pressing in years when forecasts indicate a high probability of a strong or very strong El Niño. In June 2026, the National Oceanic and Atmospheric Administration (NOAA) Climate Prediction Center (CPC) forecasting a 63% chance for a very strong El Niño during the 2026/27 rainfall season (NOAA CPC, 2026a).

Although historical approaches have successfully characterized ENSO's typical agricultural impacts across Africa (Anderson et al., 2019; Sazib et al., 2020; Coughlan de Perez et al., 2024) allowing for ENSO-based planning, seasonal outlooks that translate ENSO information into user products still typically provides generic difficult-to-use information (Lemos et al., 2012; Hansen et al., 2022), while planners (farmers, water resource managers, national agencies, humanitarian and food-security actors) need to assess and action the risk and potential impacts of heat stress, evaporative demand, the timing and reliability of the rains, including dry spells. Here we address two important questions: which of these many agriculturally relevant variables can ENSO predict, and where is that prediction trustworthy?

This paper introduces an operational analysis framework that addresses both. It converts an ENSO state, classified with the Relative Oceanic Niño Index (RONI), which removes the tropics-wide warming trend so events can be classified under a changing climate (L'Heureux et al., 2024), into gridded, analogue-composite outlooks for over a dozen agriculturally-relevant indicators. These span rainfall, the climatic and crop-specific water balance, evaporative demand, dry-spells, rainy-season timing, and heat extremes, each accompanied by a pixel-scale statistical-significance mask (and, for the frequency view, a bootstrap robustness mask). ENSO state is subdivided into categories: moderate-to-strong La Niña, weak La Niña, weak El Niño and moderate-to-strong El Niño, adapting NOAA's ENSO strength classifications (NOAA CPC, 2026b). For each of these state selections, we characterize the robustness of ENSO teleconnections using several skill score metrics, at both the grid-cell and at an aggregated sub-regional scale, to establish which indicators exhibit enough historical consistency to carry genuine predictive value. The results presented here are based on either individual grid cells or a spatially average 'core' region that exhibits the most robust impacts .

In the Southern African context, such a framework is particularly relevant as a regional climate-service support tool. Seasonal outlooks produced through regional processes such as the Southern Africa Regional Climate Outlook Forum (SARCOF) increasingly need to be complemented by indicator-specific information that is meaningful for agriculture, drought monitoring, water resources and other climate-sensitive sectors. A regional ENSO-conditioned system of this nature can therefore provide an early, long-lead layer of risk intelligence for SADC Member States, while still requiring interpretation and contextualisation by NMHSs and sector institutions at national level. In this sense, the framework is intended to complement, existing national and sub-national climate services.

2. Data and indicators

All indicators are derived from open, operational satellite-gauge and reanalysis records over 1981-2025 on the southern Africa domain (Table 1). These have relatively high spatial resolutions of 0.05 degree latitude by 0.05 to 0.625 degree longitude, enabling identification of patterns at a spatial scale that is useful for local to subnational planning. Rainfall is CHIRPS v3 (Funk et al., 2015, 2026); reference evapotranspiration (ETo) is the Hobbins et al. (2023) long-term reanalysis (FAO-56 Penman-Monteith, Allen et al., 1998; MERRA-2 forced, Gelaro et al., 2017); daily maximum 2-m air temperature (Tmax) is CHIRTS-ERA5 (Climate Hazards Center, 2025). CHIRTS-ERA5 bias-corrects ECMWF ERA5 reanalysis 0.25 degree resolution (Bell et al., 2021) data relative to 0.05 degree resolution CHIRTS temperature data (Funk et al., 2019; Verdin et al., 2020). Additional indicators were derived from these basic inputs:

- Standardized Precipitation-Evapotranspiration Index (SPEI): the standardized climatic water balance D = P – ETo (Vicente-Serrano et al., 2010). SPEI was standardized non-parametrically via the Gringorten plotting position (Farahmand & AghaKouchak, 2015), which avoids the poor distributional fit of the classic log-logistic in high-rainfall, occasionally dry areas. For consistency, we also compute the Standardized Precipitation Index (SPI; McKee et al., 1993) by the same nonparametric standardization applied to precipitation.
- Water Requirement Satisfaction Index: (WRSI; Verdin & Klaver, 2002; Senay & Verdin, 2003).
- Dry-spells(total dry-spell days and the longest dry spell, post-onset, counting only spells of at least 10 days): Our dry day definition uses a smoothed definition: a day is dry when its forward 10-day-mean rainfall is below 1 mm per day, so an isolated light-rain day does not fragment a spell; spells are counted only after season onset (defined for the daily dryspell analysis as the first rain day on which 25 mm falls over a 10-day period). Where no onset occurs in a particular season, the climatological-mean onset is used as a fallback so that years in which the season fails to establish are represented
- Rainy-season timing and duration: Rainy-season onset is the first dekad after 31 August meeting a rainfall-accumulation threshold, with a minimum of 25 mm of rainfall in the first dekad, and a total of at least 20 mm in the ensuing 2 dekads (Senay and Verdin, 2003); cessation is the last dekad before 1 June in which at least 10 mm is received following a wet event of at least 30 mm in the previous 3 dekads, and followed by a sustained dry period of at least 3 dekads; length is the onset-to-cessation span in dekads. Dekads divide each month into two ten-day periods, followed by a third dekad containing the remainder of the days in each month. We also track onset occurrence, that is, whether a season establishes at all in a given year, which carries information in the arid margins where onset is not guaranteed.
- Temperature and heat indices: mean daily Tmax, counts of days above 30 °C and 35 °C (the latter a maize-relevant heat threshold; Lobell et al., 2011), and heatwave days (Perkins & Alexander, 2013).

Indicators are computed for nine overlapping seasonal windows (OND, NDJ, DJF, JFM, FMA, MAM, DJFM, SOND and ONDJFM); we report the peak season (DJF) unless noted (the annual season-timing metrics and WRSI use ONDJFM).

3. Methods

3.1 ENSO classification

ENSO phase is classified from the NOAA CPC RONI, the 3-month running mean of Extended Reconstructed Sea Surface Temperature version 5 (ERSSTv5) anomalies in the Niño-3.4 region relative to the global tropical mean SST anomaly (L'Heureux et al., 2024). An event requires at least five consecutive overlapping 3-month seasons at or beyond ±0.5 °C, the same classification that also defines the analogue composites (Section 3.2). NOAA CPC (2026b) grades ENSO events into Weak (0.5-0.9 °C), Moderate (1.0-1.4 °C), Strong (1.5-1.9 °C) and Very Strong (≥2.0 °C) grades; for analogue selection the three highest classes are pooled into a single Moderate-to-Strong class (≥1.0 °C), giving enough analogue years for stable statistics while separating weak from stronger events, a stratification supported by evidence that stronger El Niño events shift southern-African rainfall probabilities more than weaker ones (Pomposi et al., 2018), because central Pacific atmospheric heating and precipitation, the source of the teleconnection (Gill, 1980) becomes substantially greater (Figure 9, Funk et al., 2018)

3.2 Analogue compositing

For a given forecast phase and strength, the outlook at each grid cell is the empirical distribution of the indicator across the matching analogue years (the historical years of that phase/strength). We summarize these distributions in three ways: (a) the anomaly (mean of analogue years minus the 1991-2020 climatological mean), (b) the percent of average (1991-2020 climatological mean), and (c) the frequency: the proportion of analogue years in which the indicator falls in the upper/lower tercile (1^{st}-33^{rd} and 67^{th}-100^{th} percentiles), showing only the dominant tercile. The same analysis is repeated for 20^{th} and 80^{th} quintile extremes. These results are delivered openly through the Southern Africa ENSO Explorer (https://enso.ubramplab.org).

Figures 1 and 2 show maps of response frequencies for moderate-to-stong El Niño and La Niña events. Supplemental Figures S1 and S2 show the frequency maps for all El Niño and La Niña events.

3.3 Statistical significance

Each composite anomaly, percent-of-average and frequency layer carries a mask indicating where the phase signal is distinguishable from background variability. On each map, non-significant grid-cells are shown via hatching. The composites and the frequency layers use different masking approaches. The composite mask uses a two-sided Wilcoxon-Mann-Whitney test of the analogue-phase years against all other years ($\alpha = 0.05$; after Vicente-Serrano et al., 2011). To produce a frequency-layer bootstrapped robustness mask (Knutti and Sedláček, 2013; Collins et al., 2013), at each pixel the indicator is detrended over 1981-2025 using the Theil-Sen robust trend (Sen, 1968), the median of the detrended analogue-year anomalies gives the

composite shift, and the analogue years are resampled with replacement (500 bootstrap iterations), recomputing the median each time to form the bootstrap distribution of the shift. Because the frequency map already shows a dominant tercile (a direction) at each pixel, the pixel is retained where the one-sided 95% bootstrap bound clears zero in that direction (Wilks, 2011). Under this rule, pixels whose analogue-year detrended anomalies are mixed in sign are typically hatched as weak signals, even where one tercile is nominally dominant on the frequency map.

3.4 Forecast skill

We assess out-of-sample skill with the ranked probability skill score (RPSS) of the categorical tercile forecast against an equiprobable-tercile climatology, evaluated by leave-one-out (LOO) cross-validation at each pixel (Wilks, 2011). The forecast for each held-out year is built from the remaining years only: the indicator is detrended on year and standardized, tercile boundaries are taken from the training residuals, and an ordinary-least-squares fit of the standardized indicator on RONI defines a Gaussian predictive distribution whose integral over each tercile gives the categorical probabilities for the held-out year from its RONI value. RPSS is positive when the RONI-conditioned forecast improves on climatology, zero at no improvement, and negative when it is worse. Because the predictor is the continuous RONI value, the skill spans the full ENSO range. The predictor is the observed peak-season RONI, so this is a perfect prognosis assessment and thus an upper bound on operational skill. Detrending is applied only in this skill assessment; the composites of Section 3.2 are not detrended.

We report RPSS at each pixel and as regional indices over a southern Africa response domain delineated in prior published work (Hoell et al., 2015, 2017a; Funk et al., 2016). We report two nested extents: a regional domain (12.5-42.5 E, 35-15 S) that spans the broad southern Africa El Niño response region (including its semi-arid areas), and a core domain (26.5-36 E, 27-15 S) formed as the intersection of these two delineations, where the ENSO skill is concentrated (Fig. 3). The regional and core indices are first averaged across the domain into a single annual series, which is then scored. Aggregating before scoring raises the region-wide ENSO signal and distinguishes locally-noisy from regionally-coherent skill. For the crop water balance (WRSI), areas flagged as model's no-start-of-season are excluded before averaging. Skill at the grid-cell level is summarized by the median RPSS and the fraction of grid-cells with positive skill, both taken over valid data grid cells within the response domains where the indicator is defined (excluding no-data, ocean and no-season pixels). The RPSS and other skill measures are also presented as maps, showing the spatial variation in skill. Figure 3 shows the LOO forecast skill for DJF for rainfall, ETo, SPEI and maximum temperature. Supplemental Figures S3 and S4 show forecast skills for all 12 indicators.

A complementary, deterministic view of the out-of-sample skill is the Heidke skill score. The ENSO phase is used directly as a three-category forecast (El Niño predicts the adverse tercile, neutral the near-normal, La Niña the opposite) and scored on the full 3x3 contingency table of forecast against observed tercile, over all the years.

Two agricultural quantities need a non-tercile treatment. Season onset is defined only where a season establishes, so beyond the onset date we separately score onset occurrence, the binary event of whether the season starts at all, with a leave-one-out Brier skill score: a continuous-

RONI linear-probability forecast against the observed-occurrence climatology, over the arid margin where occurrence varies (both outcomes present).

3.5 Phase-specific verification

The continuous-RONI RPSS of section 3.4 spans the whole ENSO range and therefore blends both the El Niño and La Niña phases. To characterize each phase on its own, we add four standard verification measures (Wilks, 2011; Jolliffe and Stephenson, 2012), computed separately for El Niño and La Niña. El Niño is verified against the adverse tercile of each indicator (drier, hotter, or shorter season) and La Niña against the opposite tercile (wetter, cooler or longer season); phases are defined from the peak-season DJF RONI (El Niño ≥ +0.5 °C, La Niña ≤ -0.5 °C), a single-season assignment that agrees with the Section 3.1 five-window event classification in all but one year over the 1981 to 2025 period. This skill assessment conditions on the single-season (DJF) state; the operational composites (Section 3.1) use the multi-season event classification. Each year's observed tercile is taken from the same leave-one- out, detrended definition used for RPSS, so the category is out-of-sample.

We summarize the El Niño and La Niña phases with four measures. Each measure, compared against the one-third climatological base rate, captures complementary aspects of skill. The conditional probability of the target tercile, P (target | phase), is the most directly interpretable for decision-support: how often that tercile occurs in the phase, the verification counterpart of the ENSO-conditioned frequency the operational tool displays (Mason and Goddard, 2001). The Hanssen-Kuipers (Peirce) skill score measures discrimination, the hit rate minus the false-alarm rate on the all-years contingency table (Jolliffe and Stephenson, 2012). The Brier skill score is the quadratic score of each phase used as a probabilistic forecast of its target tercile; as a single-category measure it is the most demanding of the four and is best assessed as a map, the fraction of skillful pixels varying sharply by indicator (Wilks, 2011). The rate of return is a likelihood-based score expressed as an investment return: the profit from investing in proportion to the forecast probabilities, scored against a climatological baseline; it rewards discrimination and calibration together and is zero when the forecast adds no value beyond climatology (Hagedorn and Smith, 2009)

Two of these measures are reported per pixel for the twelve indicators (Figs. S5-S6 (conditional probability) Supplemental Figure S7 shows the Heidke skill scores associated with combinations of El Niño phase/adverse outcomes versus La Niña phase/clement outcomes. Fig. S7 captures the typical primary adverse southern Africa response. Fig. S8 shows the inverse response as skillful in the north-eastern parts of the region. Supplemental Figs. S9 and S10 show responses expressed as rates-of-return.

4. Results

4.1 Frequency of the dominant tercile, by indicator, phase and strength

Results on the the ENSO explorer portal (https://enso.ubramplab.org) have adopted a common outcome orientation. Each indicator is oriented so that red identifies its adverse outcome and blue the opposite. Here 'adverse' means the drought-and-heat direction: drier, hotter, or a

shorter or later-starting season, and for the agricultural indicators, more dry-spell days or a lower WRSI. Blue marks the wetter, cooler, or longer-season outcomes. Wet-extreme hazards such as flooding are also adverse, but lie outside our single-direction convention and are not addressed here.

Using this common outcome orientation, the indicators present a coherent result (Fig. 1). For a Moderate-to-Strong El Niño, the adverse outcome is more frequent, occurring over 70% of the time in the south-central interior core for temperature, evaporative demand and the water-balance indicators, while the opposite (wetter, cooler) response is confined to the north-eastern areas (the ENSO-rainfall dipole), and to some extent, the western-central areas, particularly western Angola. Moderate-to-strong La Niña events show the opposite response, with the wetter, cooler outcome being more frequent over the same core, albeit visibly weaker and less spatially coherent, the well-known ENSO asymmetry (Mason and Goddard, 2001; Cai et al., 2025). The season-timing indicators show the weakest, least spatially coherent response throughout.

The response is also observed to sharpen with event strength. The Moderate-to-Strong frequency maps (Figs. 1, 2) are more saturated and spatially coherent than the all-events frequency maps (Figs. S1, S2), a finding similar to that made by Pomposi et al. (2018). This contrast is directly relevant to operational planning under the Moderate-to-Strong El Niño forecast for the 2026/2027 season: the stronger the forecast event, the more likely an adverse multi-indicator response, historically. Mid-June 2026 CPC forecast suggest a 90% chance of a strong El Niño event by DJF (NOAA CPC, 2026a).

4.2 Spatial patterns of forecast skill by indicator

At the grid-cell scale, ENSO-conditioned skill (RPSS, covering the ENSO range from La Niña to El Niño) in the peak season (DJF) is positive across most of the core domain, and its magnitude differs by indicator and location. Tmax, ETo and SPEI are the most skilful, with 99 to 100% of core grid cells beating climatology, and median RPSS of +0.27, +0.22 and +0.17 respectively (Table 2). Skill for ETo and Tmax are higher in the western half of the core domain, including eastern Botswana, northern South Africa and Zimbabwe. Rainfall is skillful at 88% of core grid-cells (median RPSS +0.11), and its skill is highest in the northern and eastern part of the core-domain, including southern and central Mozambique, southern Zambia, and Zimbabwe, while in the south-west of the core domain, in northern South Africa, DJF rainfall has little to no skill (Fig. 3).

The larger regional domain provides a broader overview of skill variation across southern Africa, with the larger aggregation providing a regional-level skill measure. Tmax and ETo remain skillful over the larger domain (94% of grid cells), with exclusions being south-western Angola and western south Africa for both parameters, while ETo also has low skill in central Namibia. Rainfall and SPEI also display higher skill in the northern half of the regional domain, particularly south-eastern Angola, north-eastern Namibia, south-western Zambia and northern Botswana.

WRSI skill is also highest in a northern belt across the regional domain, covering southern Angola, northern Namibia, northern Botswana, southern Zambia, and central Zimbabwe. In this area, the WRSI is free to vary, neither saturated in the wet north, nor chronically poor (or no-season) in the drier south. For onset occurrence, in the semi-arid south-west areas (including parts of

western Angola, western and central Namibia, central and western Botswana, west of central South Africa, and southern Zimbabwe), El Niño lowers the probability that a rainy-season onset occurs from about 76% under La Niña to about 59% (LOO occurrence skill: +0.12). Skill for the parameters Days > 35 ℃ and Heatwave days is higher in the western half of the regional domain, where extreme temperatures > 35 ℃ are not uncommon. Length of season responds to ENSO mainly in the more southerly parts of the domain even though the majority of pixels (60%) are not skillful, whereas the dry-spell metrics respond more in the northern parts of the region. The onset and cessation dates are near or below climatology at most pixels (onset 33%, cessation 29%), although some onset skill is observed in north-eastern parts of the region including Tanzania, northern Mozambique, and Malawi (Figure S4(g)).

With the focus on the core ENSO-influence domain, these results highlight a consistent ranking across indicators: skill is highest for the heat and evaporative-demand variables (Tmax +0.27 and ETo +0.22 median RPSS) and the moisture indices (SPEI +0.17, rainfall +0.11), intermediate for the agronomic water-balance and heat-extreme counts (WRSI, days > 35 °C, heatwave days and dry-spell totals), and lowest for the season-timing dates (onset and cessation), which sit near or below climatology.

With a focus on the core ENSO influence domain, the results highlight a consistent ranking across indicators. Skill is highest for heat and evaporative demand, followed by moisture indices (SPEI and rainfall), then intermediate for crop water balance and heat extreme, and lowest for seasonal timing metrices, which have skill near or below climatology. Aggregating over the regional domain preserves this ranking but shifts magnitudes (Table 2). Rainfall, SPEI, length of season and the heat extremes show higher regional-index skill at that extent (rainfall +0.28, SPEI +0.26), whereas ETo is higher in the core, so the core sharpens skill at focused grid-cell analysis level, while the regional index better reflects the larger-scale ENSO influence.

4.3 Seasonal evolution of forecast skill

Across the seasonal cycle, the signal, as calculated over the core domain, strengthens from the early season (OND) to a peak at the height of the rains (DJF-JFM) before fading through FMA, though skill for Tmax and ETo remain high. (Fig. 4). The strengthening of the teleconnection between OND and DJF is related to the shifting positions of the Tropical Easterly Jet and Sub-Tropical Westerly Jet, which shift south during austral summer. Temperature skill is low in OND but coherent from NDJ, and peaks at JFM; ETo and SPEI follow a similar arc, and rainfall, while noisier, follows the same progression, except for a slight dip in skill in NDJ. When viewed spatially (Fig S3), a similar progression is observed in most areas within the domain, with Tmax, rainfall, ETo and SPEI increasing from OND through DJF and JFM, before most of these decrease through FMA. For Tmax, skill remains high through DJF, JFM, and FMA (RPSS of 0.42-0.37). For ETo, RPSS scores show a decline in FMA but still relatively high skill (RPSS of 0.29). Analysis of the other skill measures – Heidke Skill Score, as well as El Niño Rate of Return, conditional probability, and True skill score, generally follow a similar pattern, although with high spatial variability (not shown).

4.4 Phase-specific verification: El Niño and La Niña

Three further verification measures, computed for each phase and shown as maps for all indicators in the supplement (Figs. S5-S8, S11, S12) expose an ENSO asymmetry; each value cited below is the median over the analysis-domain pixels. Under El Niño the conditional probability of the adverse tercile rises above the one-third base rate for several indicators, most notably for Tmax (about 0.69), ET (about 0.63), and around 0.56 for rainfall, days > 35 °C and SPEI, while the season timing indicators only slightly exceed climatology (cessation 0.38).. The TSS ranks the indicators in the same broad order as the RPSS, and the rate of return is positive only for the temperature and demand indicators under El Niño (mean Tmax +0.23, near zero for the moisture indicators and negative for the season-timing metrics). Every measure is weaker for La Niña than for El Niño: for mean Tmax the conditional probability of the phase's own target tercile falls from 0.69 to 0.57 and the rate of return falls to near zero, the same weaker-La-Niña asymmetry seen in the composites, so outlook confidence should be higher for El Niño than for La Niña events. This asymmetry holds at the domain scale, but it varies spatially: for most indicators a substantial minority of pixels (about 30 to 50% for rainfall, SPEI and ETo, nearer 15 to 30% for temperature) carry more skill under La Niña than El Niño. This highlights the need for a spatially disaggregated analysis when quantifying ENSO

4.5 Seasonal evolution of the area-averaged response

The El Niño impact deepens through the season (Fig. 5). Area-averaged rainfall over the core domain falls from near-normal in the early season (about 87% of average in OND) to about 80% at the height of the rains, while the mean daily maximum temperature anomaly rises from near zero to about +0.9 °C, both peaking at DJF-JFM. The temperature anomaly remains high in FMA. The FMA rainfall value, like at DJF-JFM, remains substantially below average, but a minor increase indicates reduced ENSO influence on rainfall past the season peak. This mirrors the progression of skill over the course of the season noted in section 4.3: the ENSO response strengthens to the peak of the rainfall season, and the indicators are most informative and skillful at that time.

4.6 Significance of the composite signal

The operational analysis displays the composite together with where it is statistically distinguishable from background variability (Fig. 6). For a Moderate-to-Strong DJF El Niño, the SPEI and rainfall composites both show the characteristic interior drying; the significance mask (hatched where not significant) indicates that drying is significant over much of the land area for SPEI (42 % of land pixels) and slightly less so for rainfall (36 %), rising to 65 % and 53 % respectively within the regional domain, in alignment with the skill results and the influence of temperatures on SPEI.

5. Discussion

The composites show a coherent north-south structure in the El Niño response (Fig. 1). The adverse outcome dominates the southern and central interior, weakens through a transition belt of low signal over central Angola, northern Zambia, northern Malawi and northern Mozambique, and then reverses to the north: over Tanzania and western Angola El Niño years tend to tilt

toward the favourable outcome (wetter, lower evaporative demand), while over central DRC the signal is largely absent. This is the regional expression of the East-Africa / Southern-Africa dipole in the ENSO rainfall teleconnection, in which a suppressed subtropical rain belt dries the summer-rainfall zone while the equatorial East African regime, often reinforced by a warm western Indian Ocean, responds with the opposite sign (Ropelewski & Halpert, 1987; Palmer et al., 2023; Steinkopf & Engelbrecht, 2025). The transition belt is where the two regimes meet and neither outcome dominates, and a more detailed analysis is required to identify sources of predictability. The analysis domains (Section 3.4) lie south of this belt, within the coherent El Niño-drying zone (Figure 1), so the regional index averages over a spatially homogeneous response region.

Several indicators show the meridional weakening during El Niño without a clean, coherent sign reversal (WRSI, the dry-spell metrics, and the extreme heat indicators). This reflects their bounded structure. WRSI saturates where the seasonal water requirement is already met in most years, so added rainfall during El Niño does not register as further WRSI improvement. The extreme heat indicators, particularly days > 35 ℃, seldom activate in much of northern half of the region, where temperatures rarely reach this level. The dry-spell metrics are already near a floor of zero in the humid north, and the wetter El Niño seasons therefore cannot reduce them further. This floor does not apply in some bimodal north-eastern areas, where a January to February break between the OND and MAM rainfall seasons means dry-spell counts are often above the zero floor.

It is worth noting that complementary rainfall, temperature and ETo responses amplify agricultural risks, especially perhaps in Botswana, Central and Southern Mozambique and Southern Zambia, where ~70% of analog years had negative outcomes (Fig. 1). These areas, along with southern Madagascar, also have large negative rainfall anomalies, on average, during moderate-to-strong El Niño events (Fig. 6). It should also be noted, however, that the entire region south of 15°S has an average SPEI anomaly of at least -0.5Z (Fig. 6). Given that the SPEI has a standard normal distribution, a -0.5Z shift increases the chance of a very low (<-2.0 SPEI) outcome two-fold, while a -1 shift increases the probability more than four-fold.

The predictability is also seasonally structured (Figs 4, S3). Skill is weak in the early season (OND), strengthens through NDJ to a peak at DJF and JFM, and fades through FMA, tracking the build-up of the ENSO response to the peak of the rains, and the subsequent reduction thereafter (Section 4.5, Fig. 5). This progression is most pronounced for rainfall and SPEI, whose skill is spatially fragmented early and late in the season, and most extensive at the peak, while ETo and temperature carry usable skill across a longer window and a wider area. The seasonal frequency composites show a similar outline - the adverse outcome footprint expands and intensifies from OND to the DJF-JFM peak before contracting (not shown), and the north-eastern favourable outcome is most evident in OND, when the East African short-rains response to El Niño is strongest. And in many areas and for several parameters, outlook confidence increases with ENSO event strength *(Fig. 1 vs S1)*, giving opportunities for improved long lead planning.

For users, the implications of these findings are important. The results show that ENSO-based predictability is not uniform across indicators, seasons and locations and this should guide how such information is interpreted in operational settings. Temperature and SPEI teleconnections

are reliable; in contrast, both predictability and skill of seasonal rainfall totals are more spatially variable, while seasonal rainfall characteristics, such as season length, timing and dry spells are even more variable. The crop water balance is regionally skillful once no-onset seasons are handled, and many areas exhibit a 60-to-70% probability of negative outcomes. In contrast, seasonal timing characteristics such as onset and cessation show comparatively weak and inconsistent skill and should therefore be treated with greater caution in operational applications.

The share of the regional domain with zero-length seasons (no onset) rises under El Niño, and the regional season-length skill carries little information about how much shorter an established season will be, we find that the regional season-length skill is low when only actual onset seasons are considered. We also find that indicator definition affects skill, a smoothed dry-spell definition recovers the regional ENSO skill that the classic consecutive-dry-day definition misses. This could be due to the reduced accuracy of CHIRPS that has been noted at daily timesteps, including discrimination of rain vs no-rain (Dinku et al., 2018; Du Plessis and Kibii, 2021). This finding highlights the utility of the smoothed dry-day approach for analysis and monitoring, moreso given its relevance for agricultural impacts – a single day of light rainfall makes little difference in crop water availability, although it breaks the consecutive-dry-day count. Ultimately, decision guidance resulting from ENSO-indicator analysis needs to be considered spatially and account for multiple parameters in the field of interest, including agriculture, water resources, and health.

Several limitations bound these claims. The analogue-composite outlook assumes the historical ENSO teleconnection is stationary, and so historical analogues are representative of future ENSO events; the relative (RONI) classification mitigates, but does not eliminate, non-stationarity, though the southern-Africa ENSO rainfall dipole has been found to remain stable in a warming climate (Steinkopf and Engelbrecht, 2025). One analysis of El Niño-driven dry seasons (Funk et al., 2018) emphasized the importance of non-adjusted Niño3.4 SSTs, which are increasing in the observations (Funk et al., 2018 - Fig. 3g) driving more extreme central Pacific precipitation responses (Funk et al., 2018 - Fig. 9a,d). Under such a view, the expected teleconnection forcing associated with the 2026/27 El Niño is likely to be very strong. Another weakness of the analog compositing approach is that it may actually underestimate temperature and temperature-related ETo values, which have been increasing over time.

The significance mask guards against over-interpreting the composite maps, but it is an in-sample detection and so can be optimistic relative to out-of-sample skill. For the frequency view, the bootstrap robustness mask additionally guards against small-sample instability, hatching where the dominant tercile could be due to chance.

An additional limitation is that this study focuses on the ENSO signal alone. Southern Africa summer rainfall is shaped by several other climate modes that can modulate the ENSO response, among them the Subtropical Indian Ocean Dipole (SIOD) (Hoell et al., 2017a), the strength and position of the Angola Low together with the mid-tropospheric Botswana High and the South Indian Ocean High (Blamey et al., 2018), variability in the tropical Atlantic, and the Southern Annular Mode (Ibebuchi, 2024). Hoell et al. (2017b) demonstrate that the influence of the SIOD-ENSO combinations extend beyond climatic variable to affect hydrological land surface variables

such as runoff and soil moisture. Because the analysis conditions seasonal outcomes on ENSO, it does not represent these modulators, which is one reason a given El Niño can over- or under-perform its composite (Blamey et al., 2018). This was the situation during the strong 1997/98 El Niño, when local conditions, an unusually strong Angola Low and unusually high regional SSTs in the western Indian and tropical South Atlantic Oceans, moderated the El Niño influence (Lyon and Mason, 2007).

Despite these limitations, ENSO remains a dominant mode of interannual summer-rainfall variability over the region (Lindesay, 1988; Pohl et al., 2018; Steinkopf and Engelbrecht, 2025). In a follow-up study, Lyon and Mason (2009) showed that event dynamical models could not reproduce the regional circulation anomalies that moderated the 1997/98 El Niño response, most notably the enhanced Angola Low and its associated Southern Hemisphere stationary-wave pattern, even when forced with observed SSTs and at a two-month coupled-model lead. ENSO can thus provide a useful tool for long-lead guidance, as it captures the dominant component of the seasonally predictable signal, even if it does not account for the whole of the region's climate variability. Moreover, the regional circulation features that have low predictability at seasonal leads become more forecastable at sub-seasonal time scales (Masukwedza et al., 2025). An ENSO-based long-lead outlook can therefore be progressively refined by these shorter-lead drivers, resulting in a multi-tier decision support framework with increasing accuracy as the season approaches (Hoskins, 2013).

6. Conclusion

This study set out to establish and communicate which ENSO-conditioned indicators are predictable over Southern Africa, and where the relationships are most reliable. We demonstrate that predictability is substantial but unevenly distributed, and that the unevenness is systematic. Temperature and evaporative demand are the most reliably predictable indicators across the widest area; the climatic water balance and rainfall totals carry usable but more spatially fragmented skill; the crop water balance is regionally informative once complete season failure is separated from variation among seasons that become established; and the season onset and cessation are only predictable in localized cases. The signal is highest in the south-central interior, reverses across the regional rainfall dipole, and is strongest at the peak of the rainfall season. Predictability is also asymmetric, being weaker for La Niña than El Niño, and it increases with event strength, so outlook confidence should be set accordingly: a point of direct relevance to the very strong El Niño forecast for the 2026/27 season.

The practical consequence is that a single "ENSO outlook" can be misleading. Guidance varies based on the specific indicator, period and location of interest. Significance and robustness masks are designed to make this reliability visible to users. Because the assessment conditions on observed ENSO state, it represents an upper bound; operational skill will be lower when ENSO forecasts are used to drive an ENSO-based guidance system such as this one, given inherent limitation in forecasts versus observations (Barnston et al., 2019) , and lower still where other modes of variability modulate the response. The integration of higher skill, longer lead ENSO-conditioned forecasts, and shorter-lead and sub-seasonal regional forecasts enables a continuum of forecasts with increasing accuracy as lead-time decreases. On the other hand, given that

current predictions for late 2026 (NOAA CPC, 2026a) suggest a 63% chance of a very strong DJF El Niño, a 32% chance of a strong El Niño and an 8% chance of a moderate El Niño it seems safe to assume that a moderate-to-strong event will occur in late 2026. In addition, the inclusion of moderate events in our composites might modestly weaken the magnitude and frequencies of expected outcomes.

The framework is regional, gridded, and meteorological, and is delivered openly through the Southern Africa ENSO Explorer (https://enso.ubramplab.org). Layered with the higher-resolution drivers that become forecastable at sub-seasonal leads, an ENSO-conditioned outlook of this kind can anchor a tiered decision-support system that improves in accuracy as the season approaches.

Acknowledgements

Drs. Magadzire, Husak, Harrison and Funk were supported by the Famine Early Warning Systems Network the U.S. Geological Survey (USGS cooperative agreement G24AC00087, New Tools for Forecasting and Monitoring Agroclimatic Conditions in the Developing World). Dr. Funk was also supported by the FEWS NET-funded University Corporation for Atmospheric Research's Enhancing Meteorological Networks Partnership (EMNP). We thank the University of Botswana's Department of Physics, School of Physical and Life Sciences, for institutional support that enabled the establishment of the Research in Applied Meteorology - Physics Laboratory (RAMP Lab), where the Southern Africa ENSO Explorer is hosted.

Author contributions

T.M. conceptualized the study, developed the methodology, wrote the analysis software, performed the formal analysis, produced the visualizations, and wrote the original draft. S.R., S.M.G., C.F., and L.H. contributed to the study's conceptualization. L.H. contributed to the methodology. C.F. and G.H., as Principal Investigators of the FEWS NET project at the University of California, Santa Barbara, provided resources and project administration. All authors reviewed, edited, and approved the final manuscript.

Data availability

The input datasets are openly available from their providers: CHIRPS v3 rainfall and CHIRTS-ERA5 maximum temperature (Climate Hazards Center), reference evapotranspiration (Hobbins et al., 2023, also available through Climate Hazards Center), and the RONI index (NOAA CPC). The analysis methodology is described in full in Section 3. The regional, gridded composite outlooks are openly viewable through the Southern Africa ENSO Explorer portal (https://enso.ubramplab.org).

References

Anderson, W.B., Seager, R., Baethgen, W., Cane, M., You, L. (2019) 'Synchronous crop failures and climate-forced production variability', *Science Advances* 5 (7), eaaw1976. doi: 10.1126/sciadv.aaw1976

Allen, R.G., Pereira, L.S., Raes, D. and Smith, M. (1998) *Crop Evapotranspiration: Guidelines for Computing Crop Water Requirements*. FAO Irrigation and Drainage Paper No. 56. Rome: Food and Agriculture Organization of the United Nations.

Barnston, A.G., Tippett, M.K., Ranganathan, M. and L'Heureux, M.L. (2019) 'Deterministic skill of ENSO predictions from the North American Multimodel Ensemble', Climate Dynamics, 53(12), pp. 7215-7234. doi: 10.1007/s00382-017-3603-3

Bell, B., Hersbach, H., Simmons, A., Berrisford, P., Dahlgren, P., Horányi, A., Muñoz-Sabater, J., Nicolas, J., Radu, R., Schepers, D., Soci, C., Villaume, S., Bidlot, J.-R., Haimberger, L., Woollen, J., Buontempo C., & Thépaut, J.-N. (2021) 'The ERA5 global reanalysis: Preliminary extension to 1950', *Quarterly Journal of the Royal Meteorological Society*, 147(741), 4186–4227. doi: 10.1002/qj.4174

Blamey, R.C., Kolusu, S.R., Mahlalela, P., Todd, M.C. and Reason, C.J.C. (2018) 'The role of regional circulation features in regulating El Niño climate impacts over southern Africa: A comparison of the 2015/16 drought with previous events', *International Journal of Climatology*, 38(11), pp. 4276-4295. doi: 10.1002/joc.5668.

Cai, W., Reason, C.J.C., Mohino, E., Rodríguez-Fonseca, B., Malherbe, J., Santoso, A., Li, X., Chikoore, H., Nnamchi, H.C. and McPhaden, M.J. (2025) 'Climate impacts of the El Niño–Southern Oscillation in Africa', *Nature Reviews Earth & Environment*. doi: 10.1038/s43017-025-00705-7.

Climate Hazards Center. (2025). CHIRTS-ERA5 Data Repository [Data set]. University of California, Santa Barbara. doi: 10.15780/G2F08J

Collins, M., Knutti, R., Arblaster, J., Dufresne, J.-L., Fichefet, T., Friedlingstein, P., Gao, X., Gutowski, W.J., Johns, T., Krinner, G., Shongwe, M., Tebaldi, C., Weaver, A.J. and Wehner, M. (2013) 'Long-term climate change: projections, commitments and irreversibility', in Stocker, T.F., Qin, D., Plattner, G.-K., Tignor, M., Allen, S.K., Boschung, J., Nauels, A., Xia, Y., Bex, V. and Midgley, P.M. (eds.) Climate Change 2013: The Physical Science Basis. Contribution of Working Group I to the Fifth Assessment Report of the Intergovernmental Panel on Climate Change. Cambridge: Cambridge University Press, pp. 1029-1136.

Coughlan de Perez, E., Anderson, W., Han, E., Masukwedza, G.I.T., Mphonyane, N. (2024) 'Detectable use of ENSO information on crop production in Southern Africa', *Climate Services* 36, 100514. doi: 10.1016/j.cliser.2024.100514

Dinku, T., Funk, C., Peterson, P., Maidment, R., Tadesse, T., Gadain, H. and Ceccato, P. (2018) 'Validation of the CHIRPS satellite rainfall estimates over eastern Africa', *Quarterly Journal of the Royal Meteorological Society*, 144(S1), pp. 292–312. doi: 10.1002/qj.3244.

Du Plessis, J.A. and Kibii, J.K. (2021) 'Applicability of CHIRPS-based satellite rainfall estimates for South Africa', *Journal of the South African Institution of Civil Engineering*, 63(3), a4. doi: 10.17159/2309-8775/2021/v63n3a4.

Farahmand, A. and AghaKouchak, A. (2015) 'A generalized framework for deriving nonparametric standardized drought indicators', *Advances in Water Resources*, 76, pp. 140-145. doi: 10.1016/j.advwatres.2014.11.012.

Funk, C., Peterson, P., Landsfeld, M., Pedreros, D., Verdin, J., Shukla, S., Husak, G., Rowland, J., Harrison, L., Hoell, A. and Michaelsen, J. (2015) 'The climate hazards infrared precipitation with stations: a new environmental record for monitoring extremes', *Scientific Data*, 2, 150066. doi: 10.1038/sdata.2015.66.

Funk, C., Harrison, L., Shukla, S., Hoell, A., Korecha, D., Magadzire, T., Husak, G. and Galu, G. (2016) 'Assessing the contributions of local and East Pacific warming to the 2015 droughts in Ethiopia and Southern Africa', *Bulletin of the American Meteorological Society*, 97(12), pp. S75-S80. doi: 10.1175/BAMS-D-16-0167.1

Funk, C., Harrison, L., Shukla, S., Pomposi, C., Galu, G., Korecha, D., Husak, G., Magadzire, T., Davenport, F., Hillbruner, C., Eilerts, G., Zaitchik, B. and Verdin, J. (2018) 'Examining the role of unusually warm Indo-Pacific sea-surface temperatures in recent African droughts', *Quarterly Journal of the Royal Meteorological Society*, 144(S1), pp. 360–383. doi: 10.1002/qj.3266.

Funk, C., Peterson, P., Peterson, S., Shukla, S., Davenport, F., Michaelsen, J., Knapp, K. R., Landsfeld, M., Husak, G., Harrison, L., Rowland, J., Budde, M., Meiburg, A., Dinku, T., Pedreros, D., & Mata, N. (2019). 'A high-resolution 1983–2016 Tmax climate data record based on infrared temperatures and stations by the Climate Hazards Center', *Journal of Climate*, 32(17), 5639–5658. doi: 10.1175/JCLI-D-18-0698.1

Funk, C., Peterson, P., Harrison, L., Saldivar, R., Landsfeld, M., Pedreros, D., Shukla, S., Fink, A.H., Davenport, F., Peterson, S.H., Turner, W., Sonnier, A., Budde, M., Tabor, K., Verdin, J., Hauzaree, D., Naim, M., Alaso, D. and Husak, G. (2026) 'The Climate Hazards Center Infrared Precipitation with Stations, Version 3', *Scientific Data*. doi: 10.1038/s41597-026-07096-4.

Gelaro, R., McCarty, W., Suarez, M.J., Todling, R., Molod, A., Takacs, L., Randles, C.A., Darmenov, A., Bosilovich, M.G., Reichle, R., Wargan, K., Coy, L., Cullather, R., Draper, C., Akella, S., Buchard, V., Conaty, A., da Silva, A.M., Gu, W., Kim, G., Koster, R., Lucchesi, R., Merkova, D., Nielsen, J.E., Partyka, G., Pawson, S., Putman, W., Rienecker, M., Schubert, S.D., Sienkiewicz, M. and Zhao, B. (2017) 'The Modern-Era Retrospective Analysis for Research and Applications, Version 2 (MERRA-2)', *Journal of Climate*, 30(14), pp. 5419-5454. doi: 10.1175/JCLI-D-16-0758.1.

Gill, A.E. (1980) 'Some simple solutions for heat-induced tropical circulation', *Quarterly Journal of the Royal Meteorological Society*, 106(449), pp. 447–462. doi:10.1002/qj.49710644905.

Hagedorn, R. and Smith, L.A. (2009) 'Communicating the value of probabilistic forecasts with weather roulette', *Meteorological Applications*, 16(2), pp. 143-155. doi: 10.1002/met.92.

Hansen, J.W., Dinku, T., Robertson, A.W., Cousin, R., Trzaska, S. and Mason, S.J. (2022) 'Flexible forecast presentation overcomes longstanding obstacles to using probabilistic seasonal forecasts', *Frontiers in Climate*, 4, 908661. doi: 10.3389/fclim.2022.908661.

Hobbins, M., Jansma, T., Sarmiento, D.P., McNally, A., Magadzire, T., Jayanthi, H., Turner, W., Hoell, A., Husak, G., Senay, G.B., Boiko, O., Budde, M., Mogane, P. and Dewes, C.F. (2023) 'A global long-term daily reanalysis of reference evapotranspiration for drought and food-security monitoring', *Scientific Data*, 10, 746. doi: 10.1038/s41597-023-02648-4.

Hoell, A., Funk, C., Magadzire, T., Zinke, J. and Husak, G. (2015) 'El Niño-Southern Oscillation diversity and Southern Africa teleconnections during austral summer', *Climate Dynamics*, 45, pp. 1583-1599. doi: 10.1007/s00382-014-2414-z.

Hoell, A., Funk, C., Zinke, J. and Harrison, L. (2017a) 'Modulation of the Southern Africa precipitation response to the El Niño Southern Oscillation by the subtropical Indian Ocean Dipole', *Climate Dynamics*, 48, pp. 2529-2540. doi: 10.1007/s00382-016-3220-6.

Hoell, A., Gaughan, A.E., Shukla, S. and Magadzire, T. (2017b) 'The hydrologic effects of synchronous El Niño-Southern Oscillation and subtropical Indian Ocean Dipole events over Southern Africa', *Journal of Hydrometeorology*, 18(9), pp. 2407-2424.

Hoskins, B. (2013) 'The potential for skill across the range of the seamless weather-climate prediction problem: a stimulus for our science', *Quarterly Journal of the Royal Meteorological Society*, 139(672), pp. 573–584. doi:10.1002/qj.1991.

Ibebuchi, C.C. (2024) 'Predictability of the atmospheric circulation patterns in Africa, south of the equator, using variations of the Southern Annular Mode and ENSO', *Theoretical and Applied Climatology*. doi: 10.1007/s00704-024-04898-7.

Jolliffe, I.T. and Stephenson, D.B. (eds.) (2012) *Forecast Verification: A Practitioner's Guide in Atmospheric Science*, 2nd edn. Chichester: John Wiley & Sons.

Knutti, R. and Sedláček, J. (2013) 'Robustness and uncertainties in the new CMIP5 climate model projections', Nature Climate Change, 3(4), pp. 369-373. doi:10.1038/nclimate1716.

Lemos, M.C., Kirchhoff, C.J. and Ramprasad, V. (2012) 'Narrowing the climate information usability gap', *Nature Climate Change*, 2(11), pp. 789–794. doi: 10.1038/nclimate1614.

Lindesay, J.A. (1988) 'South African rainfall, the Southern Oscillation and a Southern Hemisphere semi-annual cycle', *Journal of Climatology*, 8(1), pp. 17-30. doi: 10.1002/joc.3370080103.

L'Heureux, M.L., Tippett, M.K., Wheeler, M.C., Nguyen, H., Narsey, S., Johnson, N., Hu, Z.-Z., Watkins, A.B., Lucas, C., Ganter, C., Becker, E., Wang, W. and Di Liberto, T. (2024) 'A relative sea surface temperature index for classifying ENSO events in a changing climate', *Journal of Climate*, 37(4). doi: 10.1175/JCLI-D-23-0406.1.

Lobell, D.B., Banziger, M., Magorokosho, C. and Vivek, B. (2011) 'Nonlinear heat effects on African maize as evidenced by historical yield trials', *Nature Climate Change*, 1(1), pp. 42-45. doi: 10.1038/nclimate1043.

Lyon, B., and S. J. Mason, (2007) 'The 1997/98 summer rainfall season in southern Africa. Part I: Observations', *Journal of Climate*, 20(20), 5134–5148. doi: 10.1175/JCLI4225.1

Lyon, B., and S. J. Mason (2009) 'The 1997/98 summer rainfall season in southern Africa. Part II: Model simulations and coupled model forecasts', *Journal of Climate*, 22(13), 3802–3818. doi: 10.1175/2009JCLI2600.1

Mason, S.J. and Goddard, L. (2001) 'Probabilistic precipitation anomalies associated with ENSO', *Bulletin of the American Meteorological Society*, 82(4), pp. 619-638. doi: 10.1175/1520-0477(2001)082<0619:PPAAWE>2.3.CO;2.

Masukwedza, G.I.T., Lazenby, M., Mwangi, E. and Todd, M.C. (2025) 'Assessing the subseasonal forecasting skill of extreme agrometeorologically relevant dry spells over Southern Africa'. *Climate Dynamics*, 63(4), 199. doi: 10.1007/s00382-025-07674-z

McKee, T.B., Doesken, N.J. and Kleist, J. (1993) 'The relationship of drought frequency and duration to time scales', *Proceedings of the 8th Conference on Applied Climatology*, Anaheim, CA, 17–22 January 1993. Boston, MA: American Meteorological Society, pp. 179–184.

NOAA CPC (2026a) El Niño/Southern Oscillation (ENSO) Diagnostic Discussion, issued 11 June 2026. Available at: https://web.archive.org/web/20260617090708/https://www.cpc.ncep.noaa.gov/products/analysis_monitoring/enso_advisory/ensodisc.shtml (Accessed: 17 June 2026).

NOAA CPC (2026b) Relative Oceanic Niño Index (RONI): ENSO strength classifications. Available at: https://www.cpc.ncep.noaa.gov/products/analysis_monitoring/enso/roni/strengths.php (Accessed: 28 June 2026).

Palmer, P.I., Wainwright, C.M., Dong, B., Maidment, R.I., Wheeler, K.G., Gedney, N., Hickman, J.E., Madani, N., Folwell, S.S., Abdo, G., Allan, R.P., Black, E.C.L., Feng, L., Gudoshava, M., Haines, K., Huntingford, C., Kilavi, M., Lunt, M.F., Shaaban, A. and Turner, A.G. (2023) 'Drivers and impacts of Eastern African rainfall variability', *Nature Reviews Earth & Environment*, 4(4), pp. 254–270. doi: 10.1038/s43017-023-00397-x.

Perkins, S.E. and Alexander, L.V. (2013) 'On the measurement of heat waves', *Journal of Climate*, 26(13), pp. 4500-4517. doi: 10.1175/JCLI-D-12-00383.1.

Pohl, B., Dieppois, B., Cretat, J., Lawler, D. and Rouault, M. (2018) 'From synoptic to interdecadal variability in southern African rainfall: toward a unified view across time scales', *Journal of Climate*, 31(15), pp. 5845-5872. doi: 10.1175/JCLI-D-17-0405.1.

Pomposi, C., Funk, C., Shukla, S., Harrison, L. and Magadzire, T. (2018) 'Distinguishing southern Africa precipitation response by strength of El Niño events and implications for decision-making', *Environmental Research Letters*, 13(7), 074015. doi: 10.1088/1748-9326/aacc4c.

Ropelewski, C.F. and Halpert, M.S. (1987) 'Global and regional scale precipitation patterns associated with the El Niño/Southern Oscillation', *Monthly Weather Review*, 115(8), pp. 1606-1626.

Sazib, N., Mladenova, I.E. and Bolten, J.D. (2020) 'Assessing the impact of ENSO on agriculture over Africa using Earth observation data', *Frontiers in Sustainable Food Systems*, 4, 509914. doi: 10.3389/fsufs.2020.509914.

Sen, P.K. (1968) 'Estimates of the regression coefficient based on Kendall's tau', Journal of the American Statistical Association, 63(324), pp. 1379-1389.

Senay, G.B. and Verdin, J. (2003) 'Characterization of yield reduction in Ethiopia using a GIS-based crop water balance model', *Canadian Journal of Remote Sensing*, 29(6), pp. 687-692. doi: 10.5589/m03-039.

Steinkopf, J. and Engelbrecht, F. (2025) 'The El Niño-Southern Oscillation teleconnection to southern Africa in a changing climate', *Environmental Research Letters*, 20. doi: 10.1088/1748-9326/ade60e.

Verdin, A., Funk, C., Peterson, P., Landsfeld, M., Tuholske, C. and Grace, K. (2020) 'Development and validation of the CHIRTS-daily quasi-global high-resolution daily temperature data set', *Scientific Data*, 7, 303. doi: 10.1038/s41597-020-00643-7.

Verdin, J. and Klaver, R. (2002) 'Grid-cell-based crop water accounting for the famine early warning system', *Hydrological Processes*, 16(8), pp. 1617-1630. doi: 10.1002/hyp.1025.

Vicente-Serrano, S.M., Begueria, S. and Lopez-Moreno, J.I. (2010) 'A multiscalar drought index sensitive to global warming: the standardized precipitation evapotranspiration index - SPEI', *Journal of Climate*, 23(7), pp. 1696-1718. doi: 10.1175/2009JCLI2909.1.

Vicente-Serrano, S.M., Lopez-Moreno, J.I., Gimeno, L., Nieto, R., Moran-Tejeda, E., Lorenzo-Lacruz, J., Begueria, S. and Azorin-Molina, C. (2011) 'A multiscalar global evaluation of the impact of ENSO on droughts', *Journal of Geophysical Research: Atmospheres*, 116, D20109. doi: 10.1029/2011JD016039.

Wilks, D.S. (2011) *Statistical Methods in the Atmospheric Sciences*, 3rd edn. International Geophysics Series, Vol. 100. Oxford: Academic Press.

Figures and tables

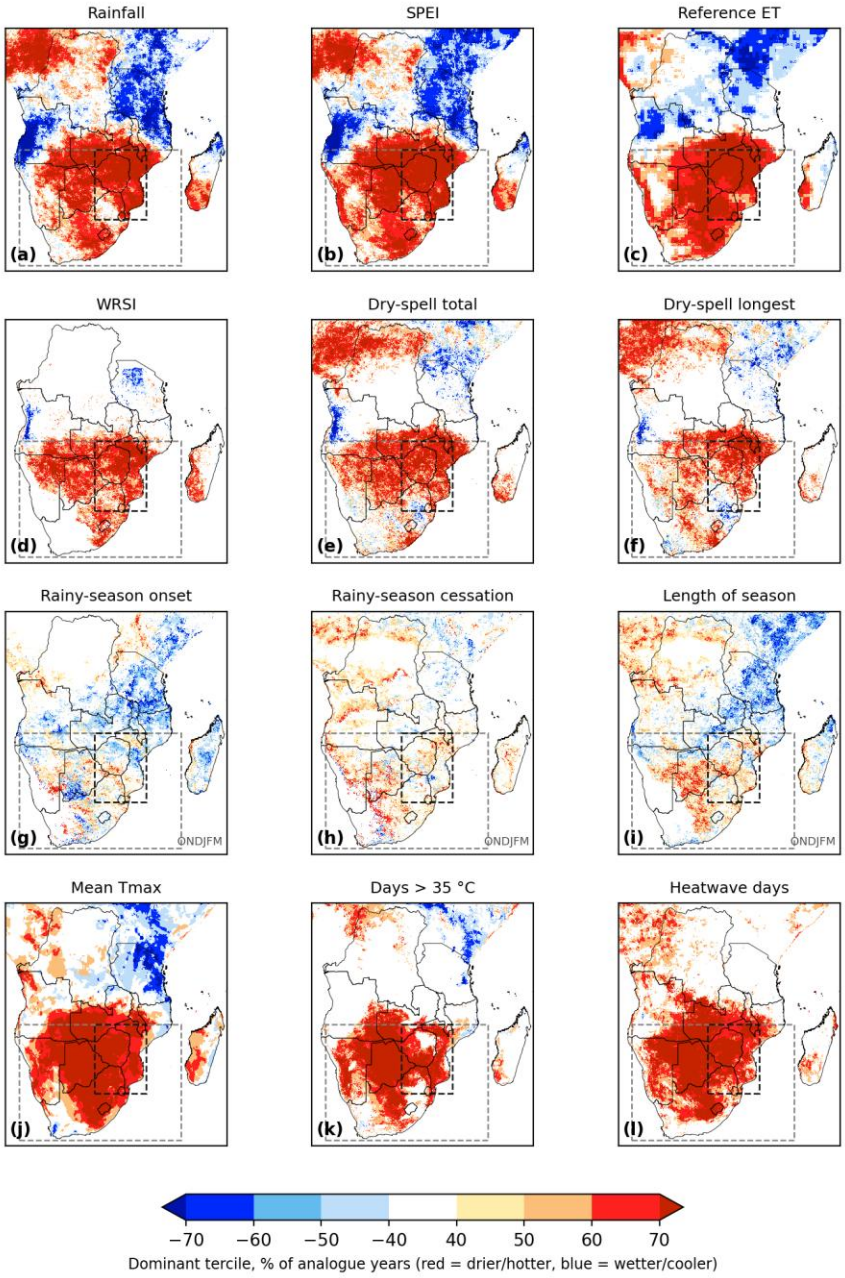

Fig. 1. Percent frequency of occurrence of the dominant tercile across twelve indicators during Moderate-to-Strong El Niño (DJF; ONDJFM for the annual season-timing metrics), the tercile frequency are shown with a common outcome orientation: red = the adverse outcome (drier, hotter, or a shorter season) occurs in more analogue years; blue = the opposite (wetter, cooler, longer season). The dashed boxes mark the regional domain (grey) and the core domain (black) (Section 3.4). Hatching marks pixels where the frequency signal is not robust (the bootstrap 95% confidence interval of the detrended median shift includes zero; Section 3.3).

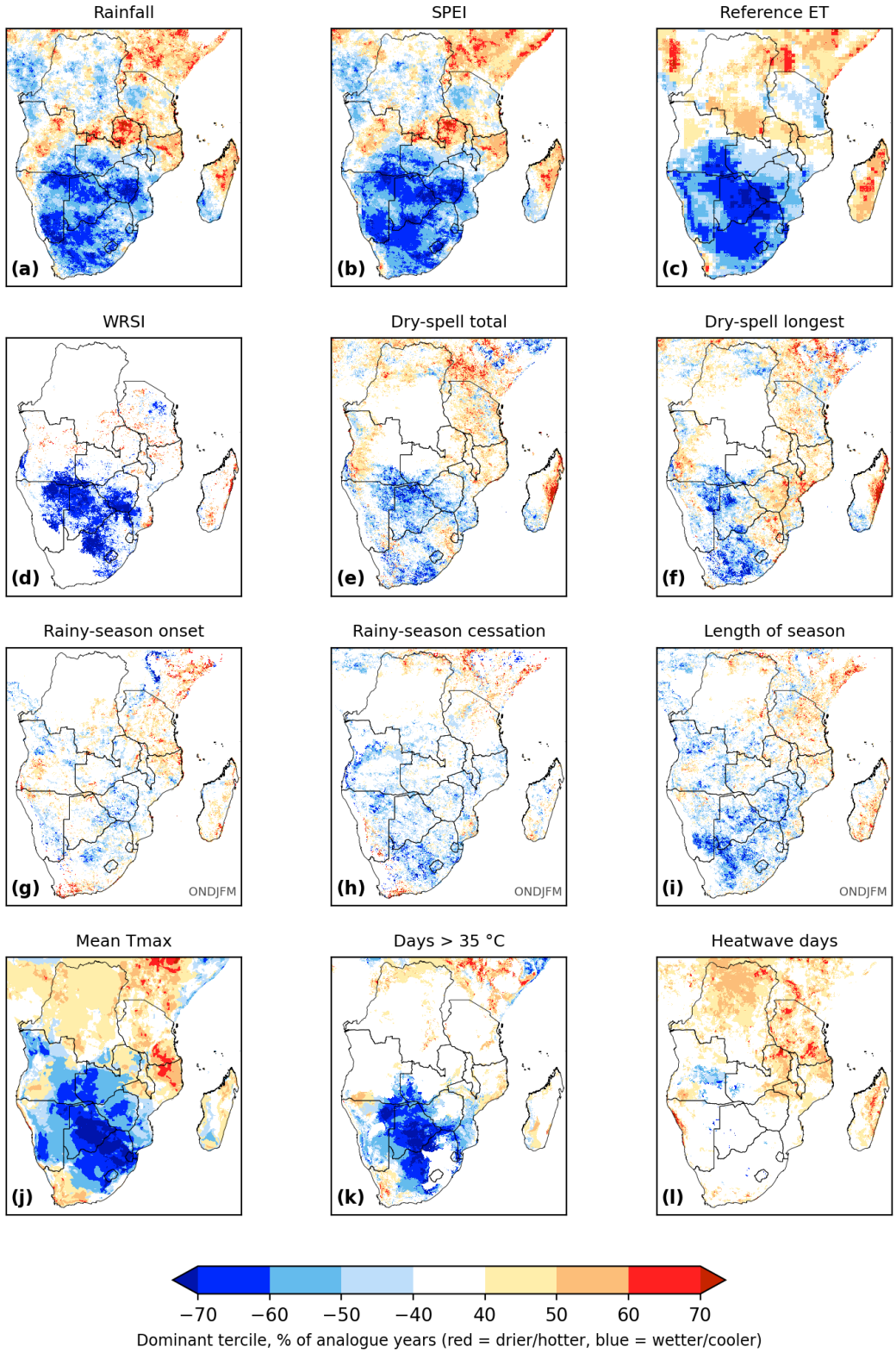

Fig. 2. Same as Fig. 1, but for Moderate-to-Strong La Niña

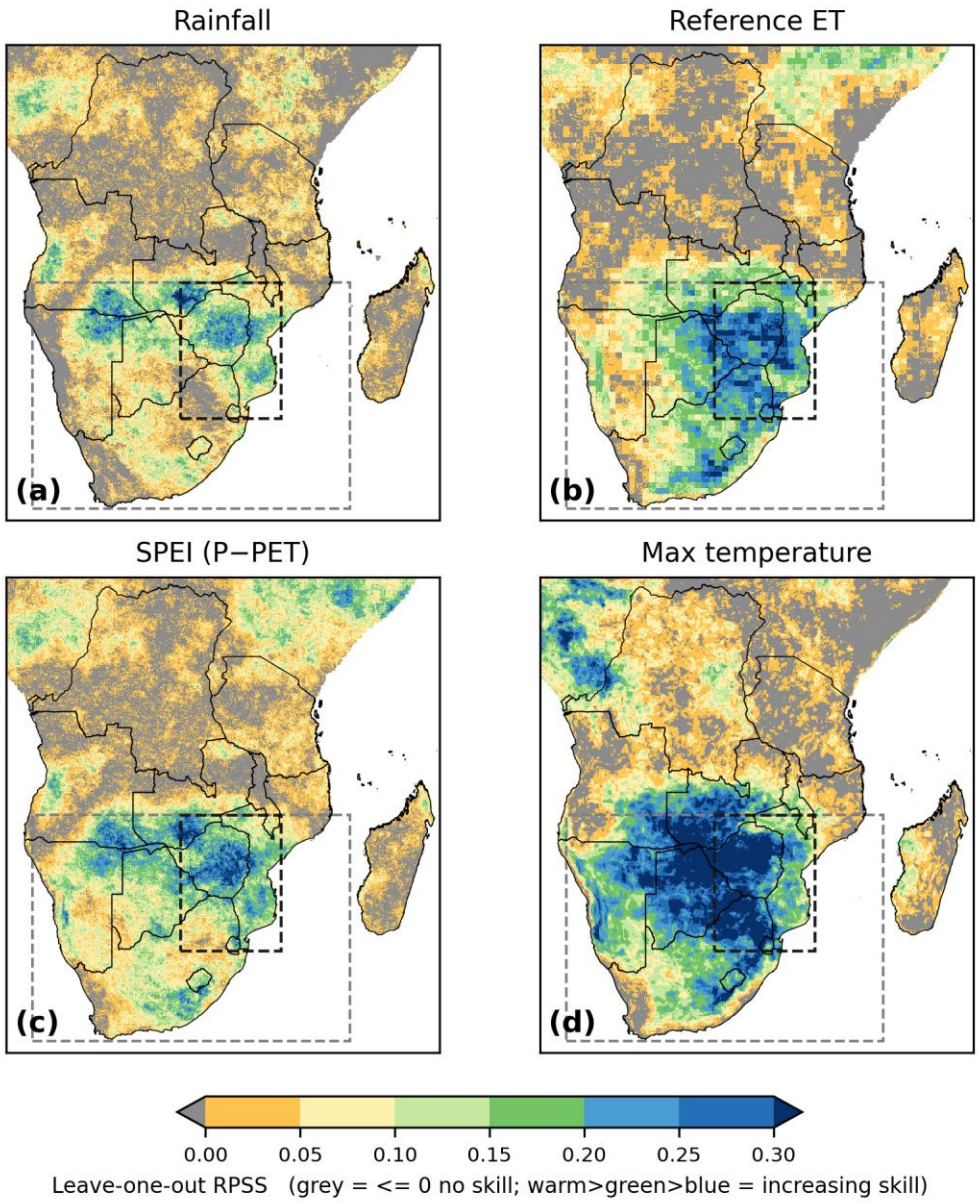

Fig. 3. Grid-cell scale leave-one-out forecast skill (RPSS vs climatology), DJF, for the four main parameters (rainfall, reference ET, SPEI, maximum temperature). Warm to green to blue colours indicate increasing skill above climatology; grey marks no skill. Skill is higher in the core domain and is coherent for temperature and reference ET, and more fragmented for rainfall and SPEI.

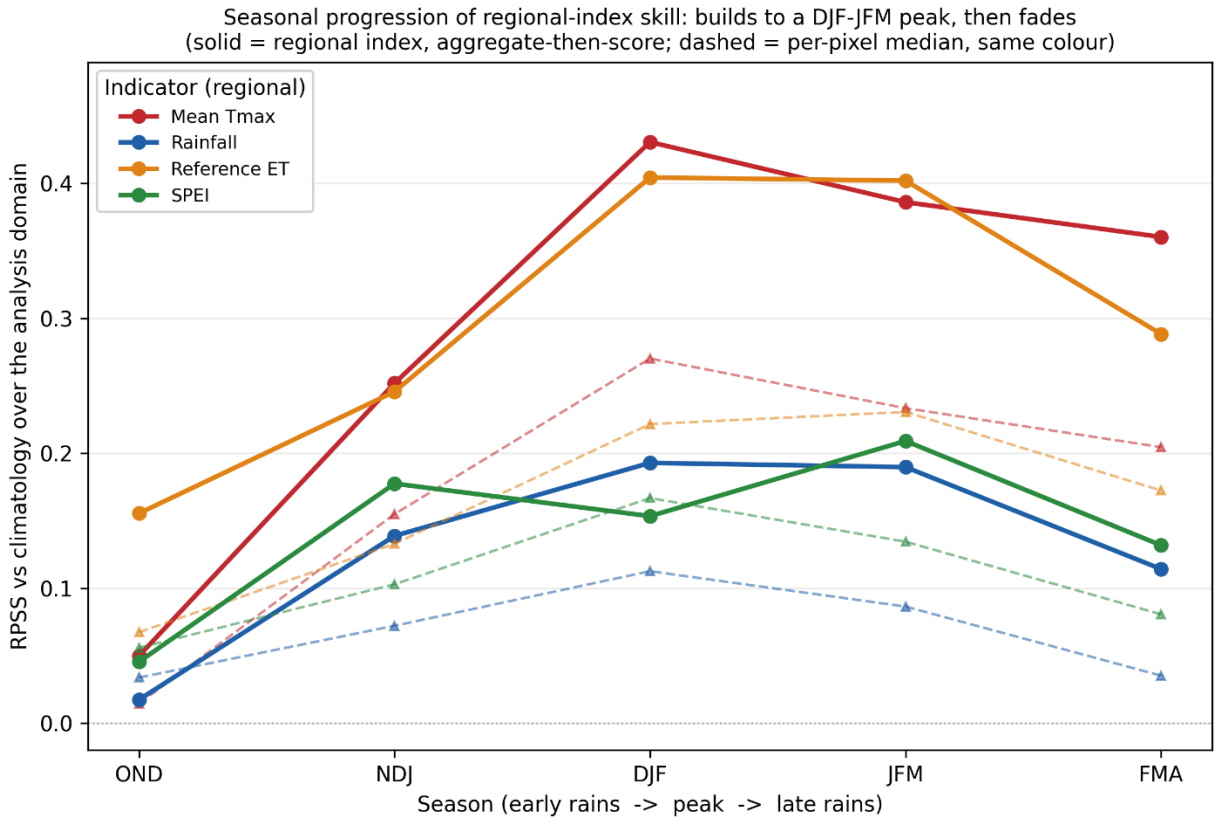

Fig. 4. Seasonal evolution of regional LOO RPSS, comparing Tmax (red), rainfall (blue), reference evapotranspiration (orange) and SPEI (green), for OND, NDJ, DJF, JFM and FMA. Skill builds to a DJF-JFM peak before fading through FMA, though skill for Tmax and reference evapotranspiration remain high. The solid lines show the regional index, while the dashed lines shows the median of all pixels over the core domain using the same colors as the dashed lines

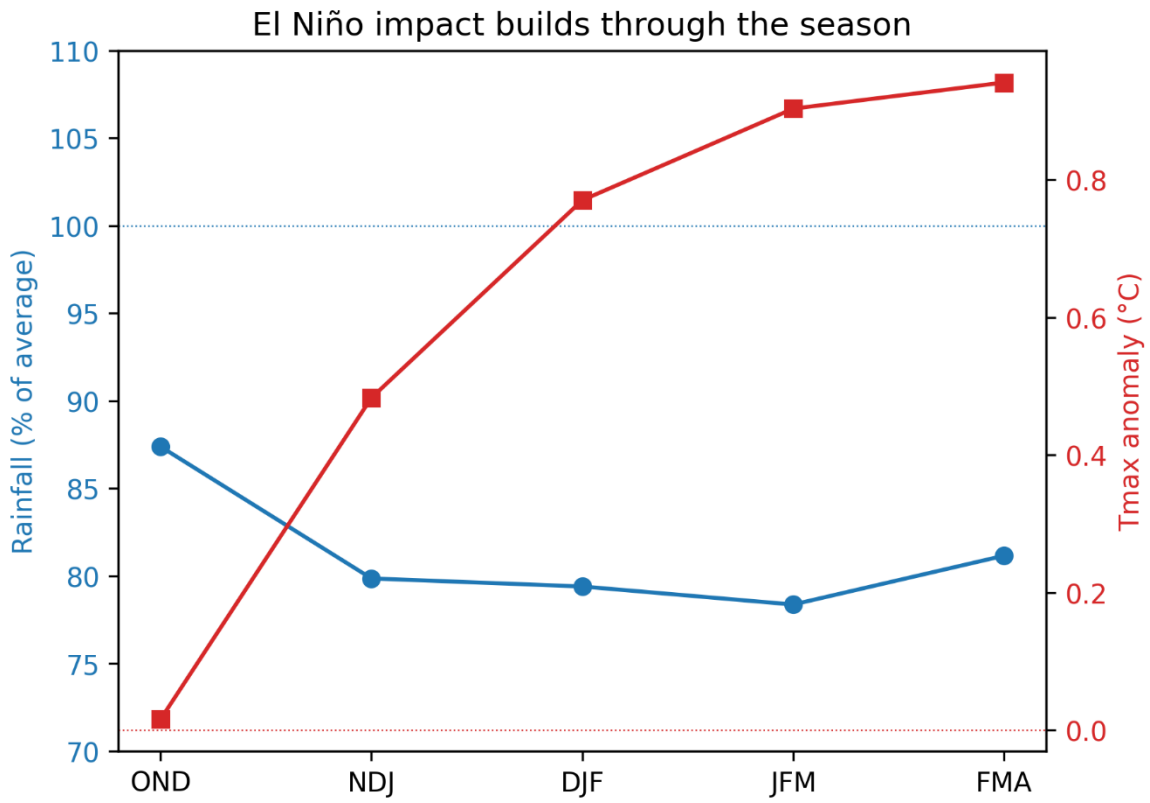

Fig. 5. El Niño impact increases through the season. Rainfall as a percentage of the long-term average (blue, left axis) and the mean daily maximum temperature anomaly (red, right axis), both averaged over the core domain, and composited over all El Niño years, by season from the early rains (OND) to the late season (FMA). Both rainfall and temperature anomalies during El Niño strengthen through the season, reaching a peak at DJF/JFM.

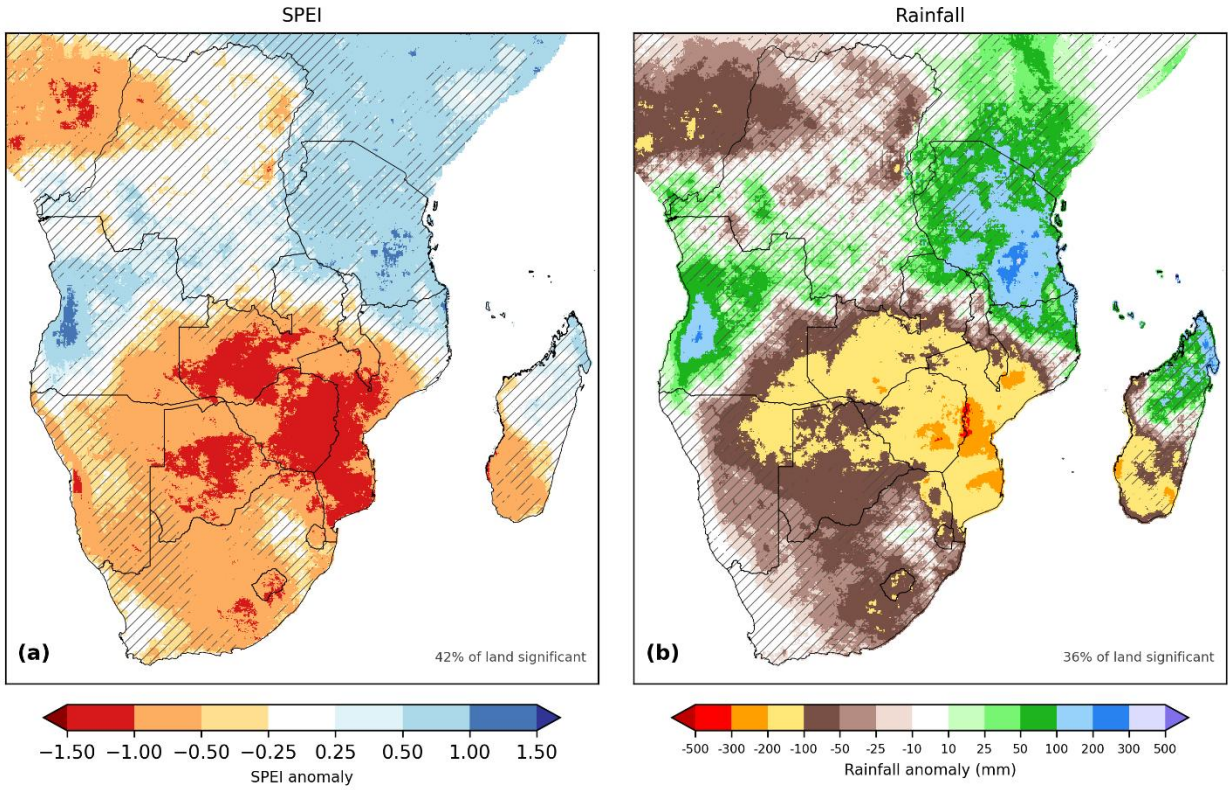

Fig. 6. Composite Moderate-to-Strong El Niño impact (DJF) for (a) SPEI and (b) rainfall: the mean anomaly over Moderate-to-Strong El Niño years, shown in the platform's colour scheme. Hatching marks pixels where the ENSO signal is not statistically significant.

Indicator	**Theme**	**Variable**	**Temporal basis**	**El Niño adverse direction**
Rainfall	Meteorological	Seasonal total rainfall (mm)	DJF	drier (lower)
SPI	Meteorological	Standardized Precipitation Index (rainfall)	DJF	drier (lower)
SPEI	Meteorological	Standardized Precipitation-Evapotranspiration Index (rainfall, ETo)	DJF	drier (lower)
Reference ET	Meteorological	Reference evapotranspiration	DJF	higher demand
WRSI	Agricultural	Crop water-satisfaction index	seasonal	lower satisfaction
Onset occurrence	Agricultural	Probability the season establishes	seasonal	less likely to start
Dry-spell total	Agricultural	Total dry-spell days (smoothed)	DJF	more dry days
Dry-spell longest	Agricultural	Longest dry spell (smoothed)	DJF	longer spell
Rainy-season onset	Agricultural	Onset dekad (where season starts)	seasonal	later onset
Rainy-season cessation	Agricultural	Cessation dekad	seasonal	earlier cessation

Length of season	Agricultural	Season length (dekads)	seasonal	shorter season
Mean Tmax	Meteorological	Mean daily maximum temperature	DJF	hotter (higher)
Days > 30 C	Heat	Count of days Tmax > 30 C	DJF	more hot days
Days > 35 C	Heat	Count of days Tmax > 35 C	DJF	more hot days
Heatwave days	Heat	Heatwave day count	DJF	more heatwave days

Table 1. Indicators assessed, grouped by theme (the variable measured, its temporal basis, the direction of the adverse El Niño response

Indicator	**Median RPSS (core)**	**% pixels > 0 (core)**	**Regional-index RPSS (core)**	**Median RPSS (regional)**	**% pixels > 0 (regional)**	**Regional-index RPSS (regional)**	**Period**
Rainfall	0.11	87.6	0.19	0.07	79.8	0.28	DJF
SPEI	0.17	98.7	0.15	0.12	93.6	0.26	DJF
Reference ET	0.22	99.9	0.40	0.15	93.8	0.26	DJF
WRSI	0.06	75.4	0.20	0.06	75.0	0.32	seasonal
Onset occurrence*	n/a	n/a	n/a	0.00	52.6	0.12	seasonal
Dry-spell total	0.04	71.1	0.16	0.03	68.2	0.17	DJF
Dry-spell longest	-0.01	43.2	0.02	-0.01	42.8	0.04	DJF
Rainy-season onset	-0.02	32.8	0.07	-0.03	30.2	-0.06	seasonal
Rainy-season cessation	-0.03	29.3	0.00	-0.03	27.8	-0.02	seasonal
Length of season**	-0.01	40.0	0.17	-0.02	36.2	0.29	seasonal
Mean Tmax	0.27	100.0	0.43	0.21	94.4	0.44	DJF
Days > 30 C	0.19	91.9	0.34	0.12	83.9	0.39	DJF
Days > 35 C	0.12	81.3	0.37	0.13	79.6	0.39	DJF
Heatwave days	0.04	72.4	0.16	0.07	75.9	0.30	DJF

Table 2. Leave-one-out skill (RPSS, against climatology) of each indicator's DJF tercile forecast from the continuous RONI predictor, over the response regions (Section 3.4). For each indicator the median grid-cell RPSS, the fraction of skillful pixels, and the regional-index RPSS (the area-mean series scored, aggregate first) are given for the core domain (primary) and, for comparison, the broader regional domain. The two are nested published delineations of the Southern Africa response region (Hoell et al., 2015, 2017a; Funk et al., 2016), the core being their intersection.

** Onset occurrence is a binary event: the regional value is the leave-one-out occurrence skill and the grid-cell value is the occurrence Brier skill over the variable-onset zone.*

*** The regional length-of-season skill reflects the spatial extent of season failure, not gradations of length among seasons that occur (see Discussion)*

Supplementary Figures

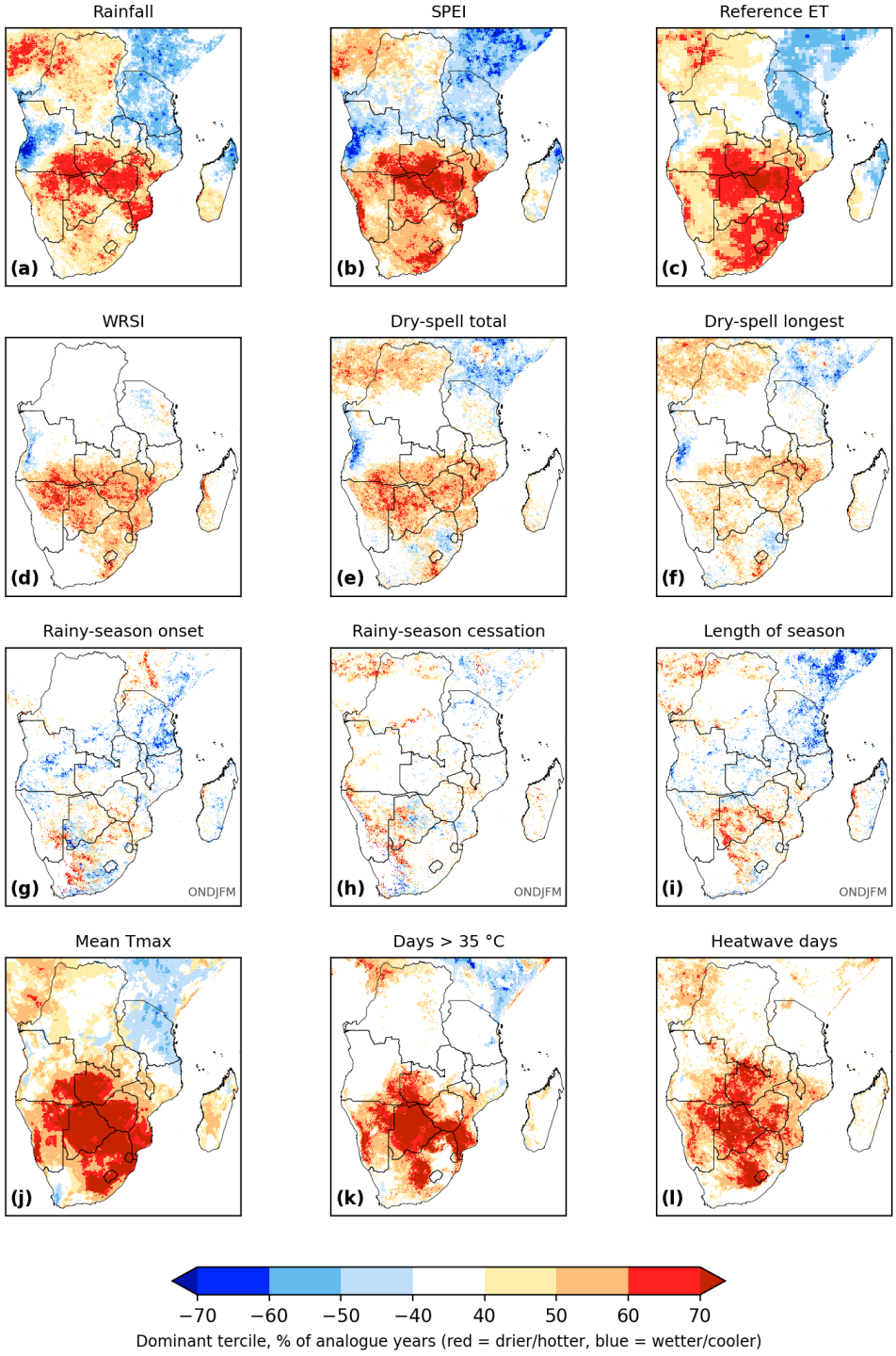

Fig. S1. As Fig. 1 but for all El Niño events (RONI ≥ 0.5 °C); the all-strength response, compared with the Moderate-to-Strong main-text figure Fig. 1 to see the strength increasing for stronger El Niño events.

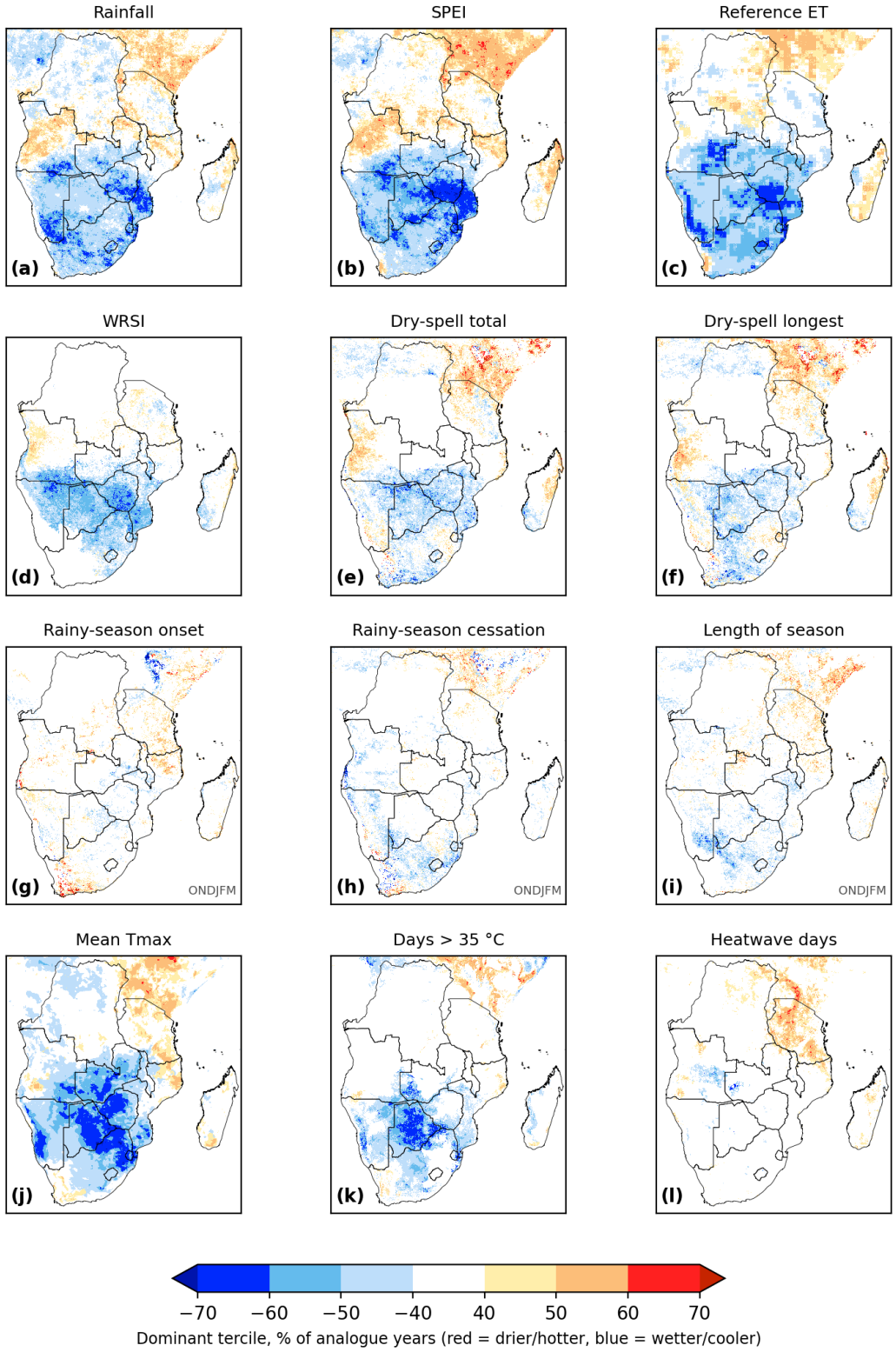

Fig. S2. As Fig. 2 but for all La Niña events (RONI ≤ -0.5 °C); the all-strength response, compared with the Moderate-to-Strong main-text figures to see the strength sharpening.

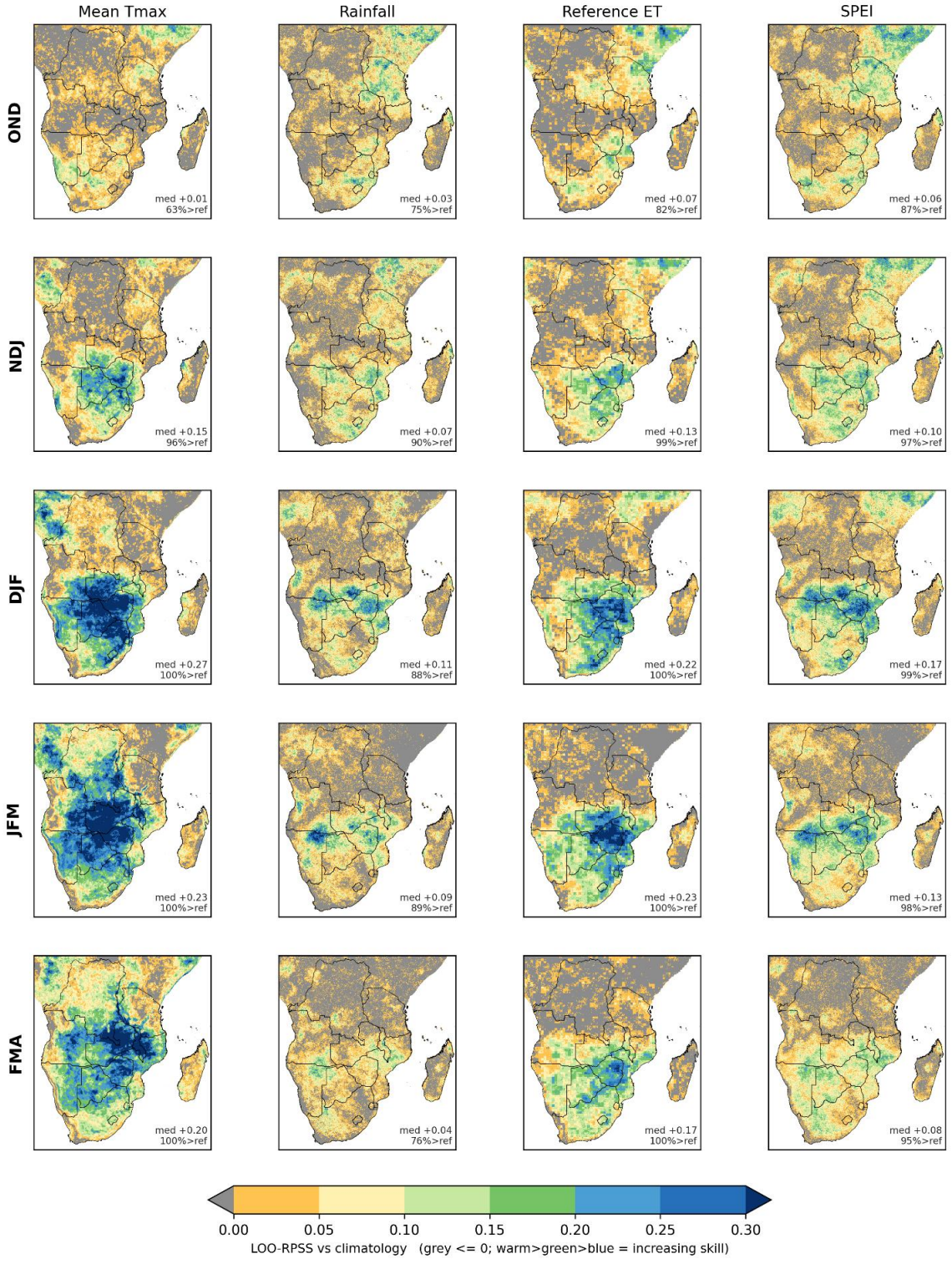

Fig. S3. Seasonal evolution of grid-cell Leave-one-out (LOO) RPSS, comparing, from left to right, Tmax, rainfall, reference evapotranspiration and SPEI, for OND, NDJ, DJF, JFM and FMA. Skill builds to a DJF-JFM peak before fading through FMA.

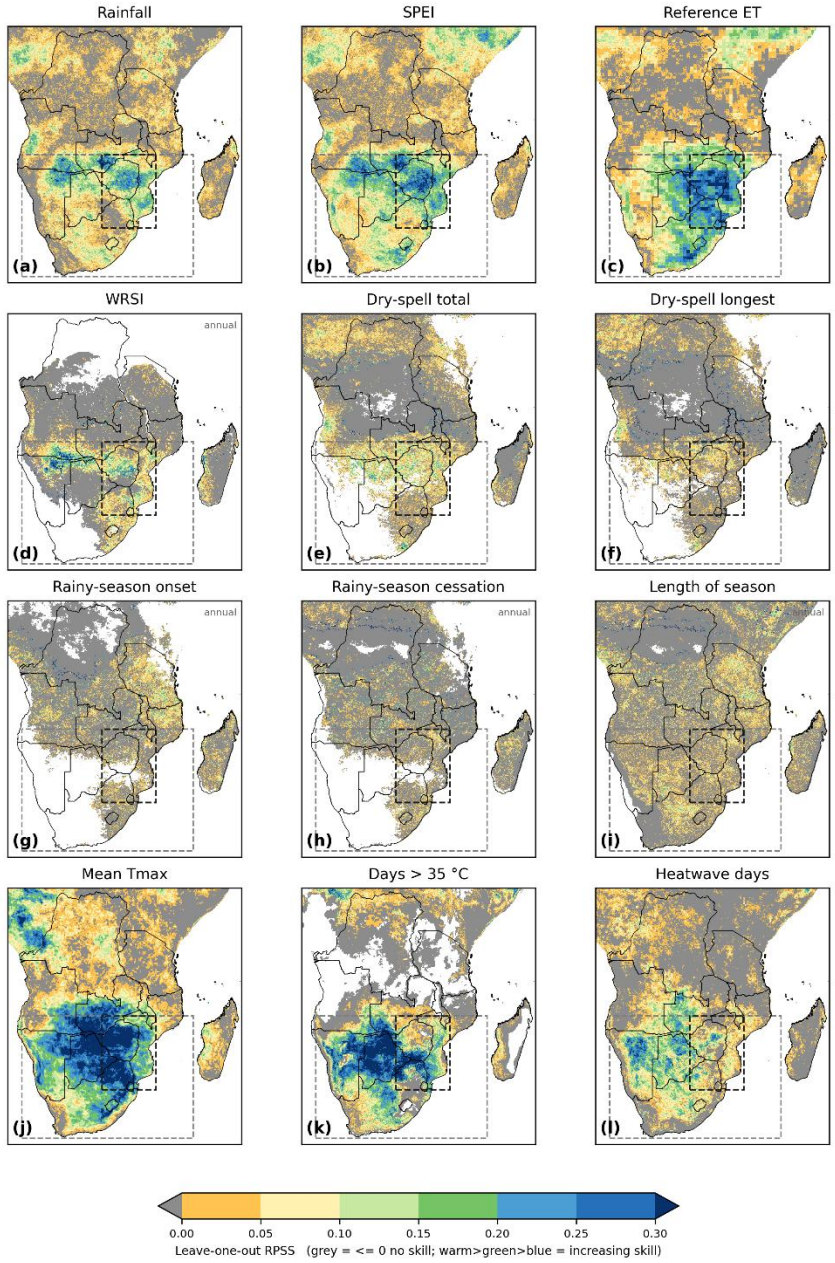

Fig. S4. Grid-cell scale leave-one-out forecast skill (RPSS vs climatology) for the twelve indicators of Figs. 1, DJF (seasonal for WRSI and the season-timing metrics). Warm to green to blue marks increasing skill above climatology; grey marks no skill. This is the skill complement to the frequency overview (Fig. S1 and S2): it shows how much of each indicator's response is predictable.

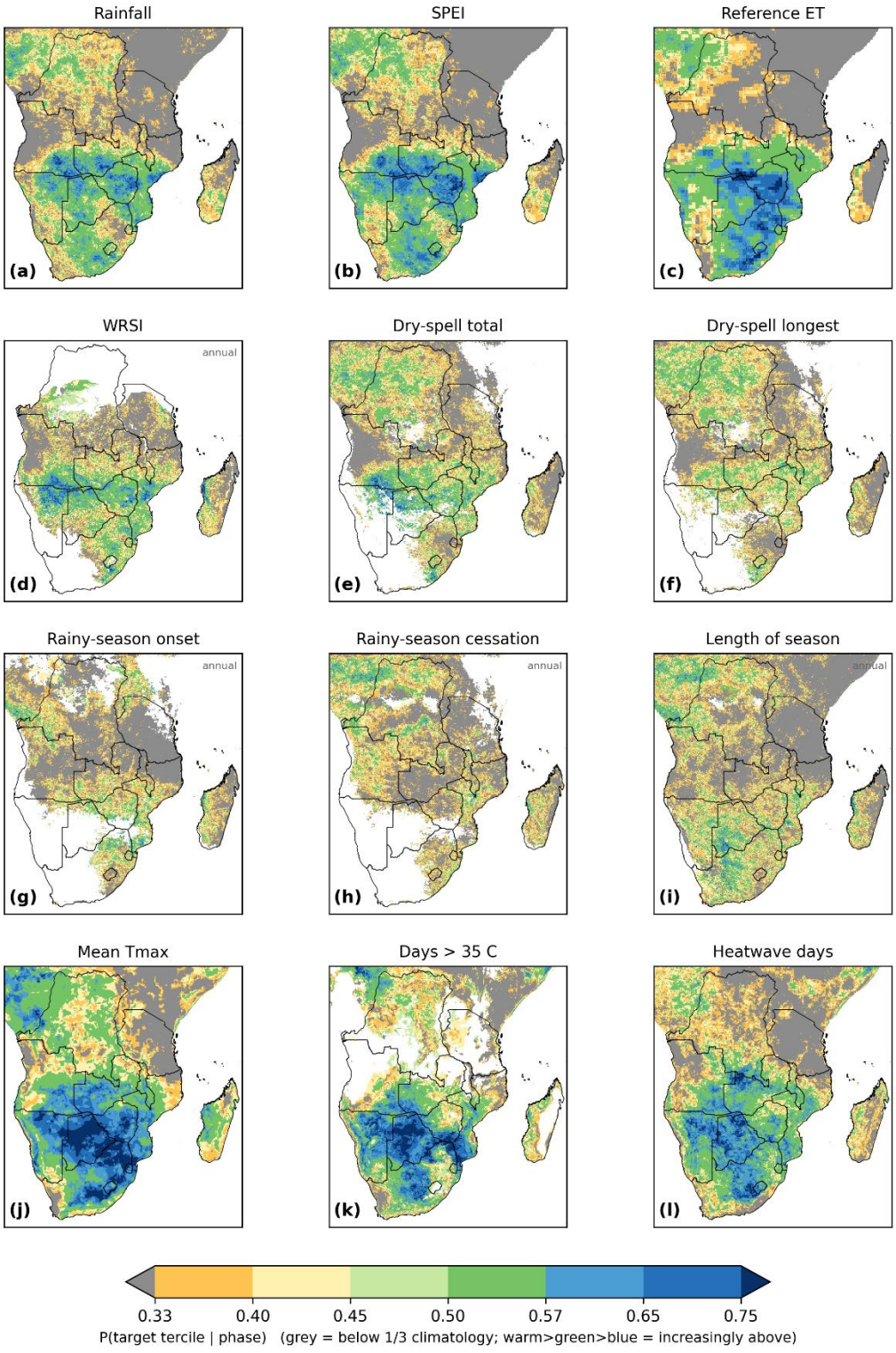

Fig. S5. Phase-specific conditional probability of the target tercile, P(target | phase), for El Niño, over twelve indicators, targetting the adverse tercile (drier, hotter, shorter season). Grey marks below the 1/3 climatological base rate; warm to green to blue marks an increasingly stronger signal above it.

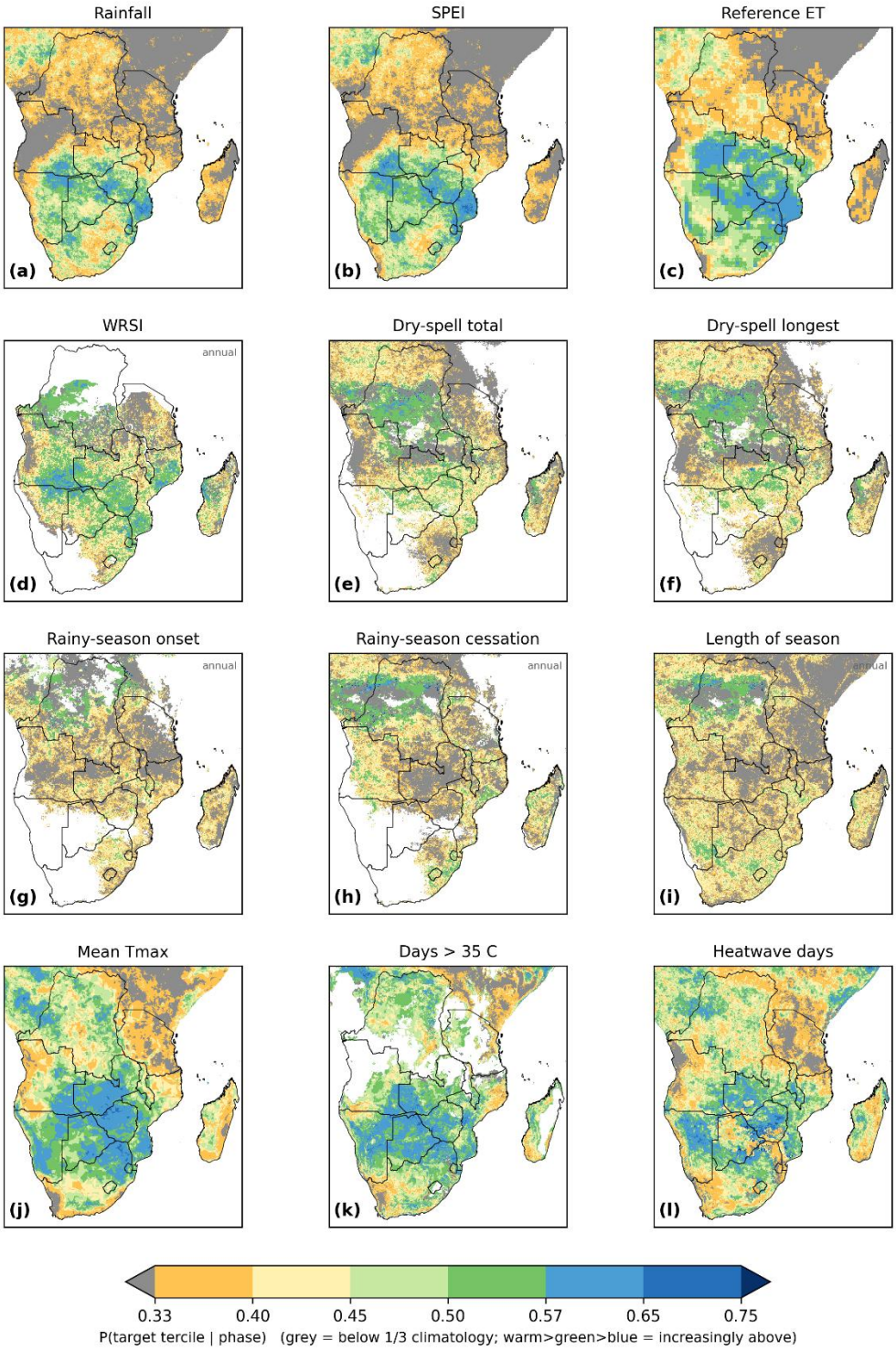

Fig. S6. Similar to Fig S5, but for La Niña. Phase-specific conditional probability of the target tercile, P(target | phase), for Niña, over twelve indicators, targetting the favourable tercile(wetter, cooler). Grey marks below the 1/3 climatological base rate; warm to green to blue marks an increasingly stronger signal above it.

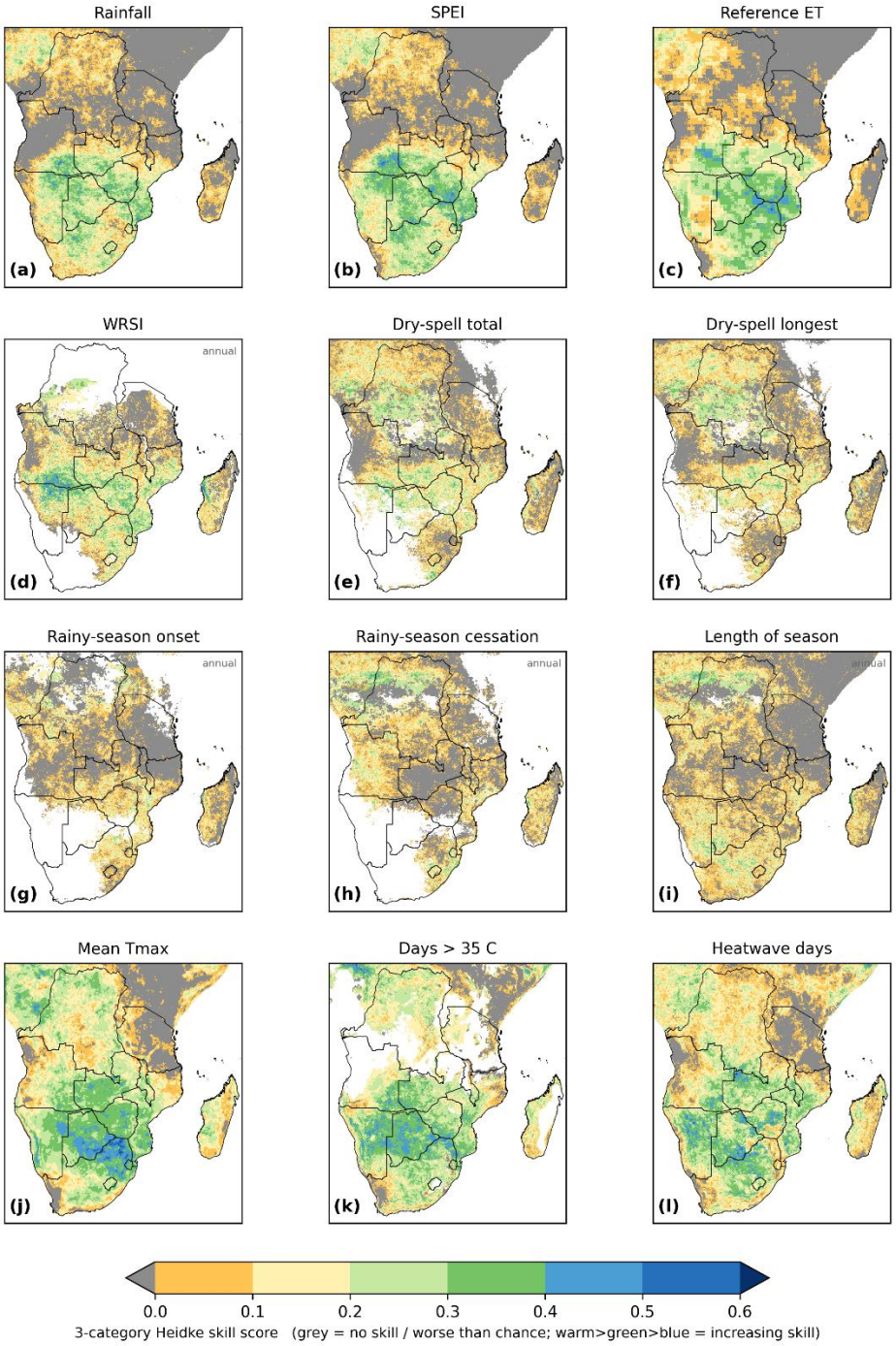

Fig. S7. Phase-specific Heidke skill score of the ENSO phase used as a deterministic tercile forecast, under a canonical orientation. El Niño predicts the adverse tercile, neutral the near-normal, La Niña the opposite). Grey marks no skill (worse than chance); warm to green to blue marks increasing skill, on the same all-years two-by-two table; chance-corrected accuracy, blue beats chance.

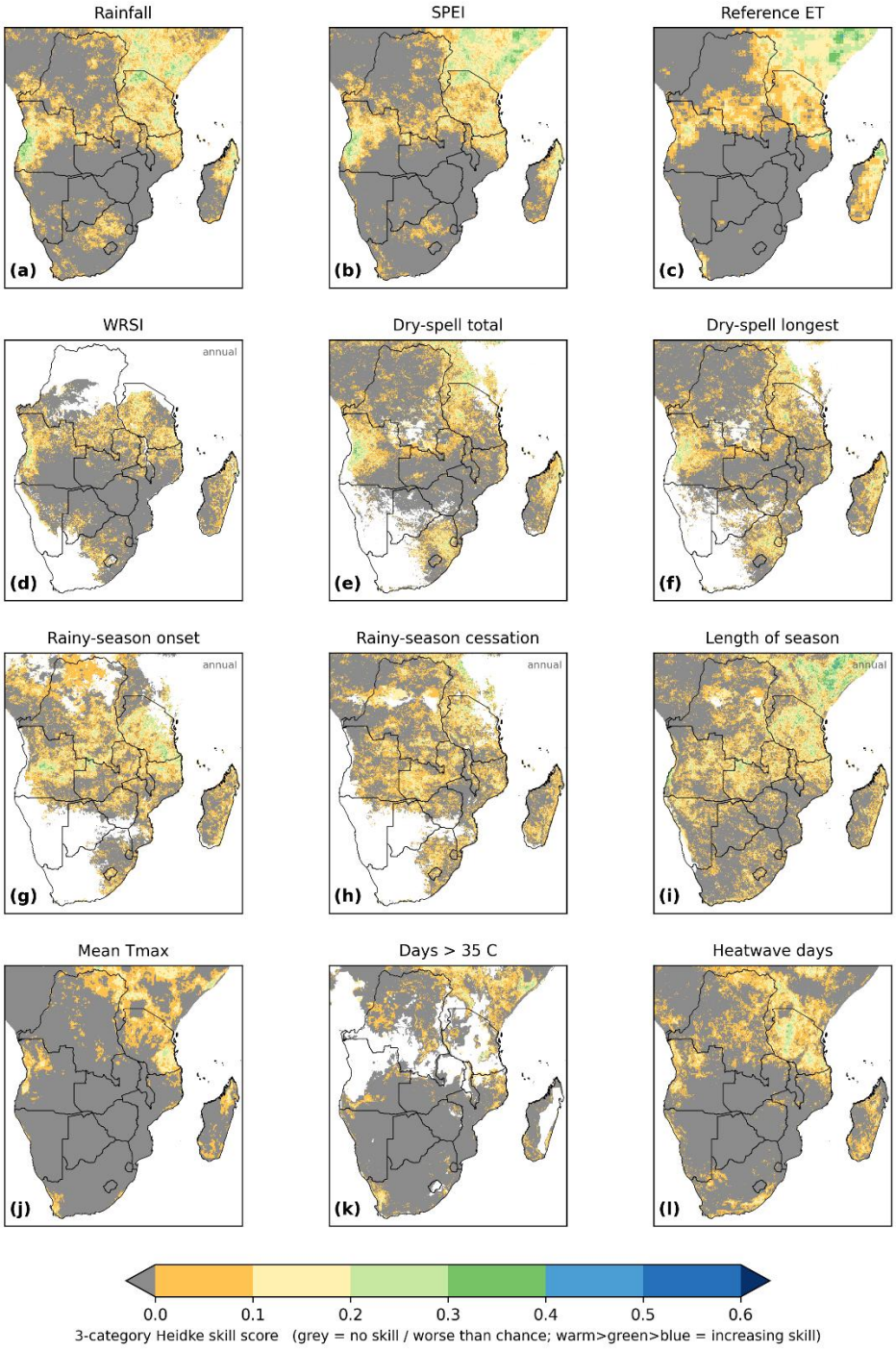

Fig. S8. Similar to Fig S7, but for the reverse orientation. Phase-specific Heidke skill score of the ENSO phase used as a deterministic tercile forecast, under a reverse orientation. El Niño predicts the favourable tercile, neutral the near-normal, La Niña the adverse. This reverse orientation lets areas with the inverse ENSO-rainfall response register as skillful. Grey marks no skill (worse than chance); warm to green to blue marks increasing skill, on the same all-years two-by-two table; chance-corrected accuracy, blue beats chance.

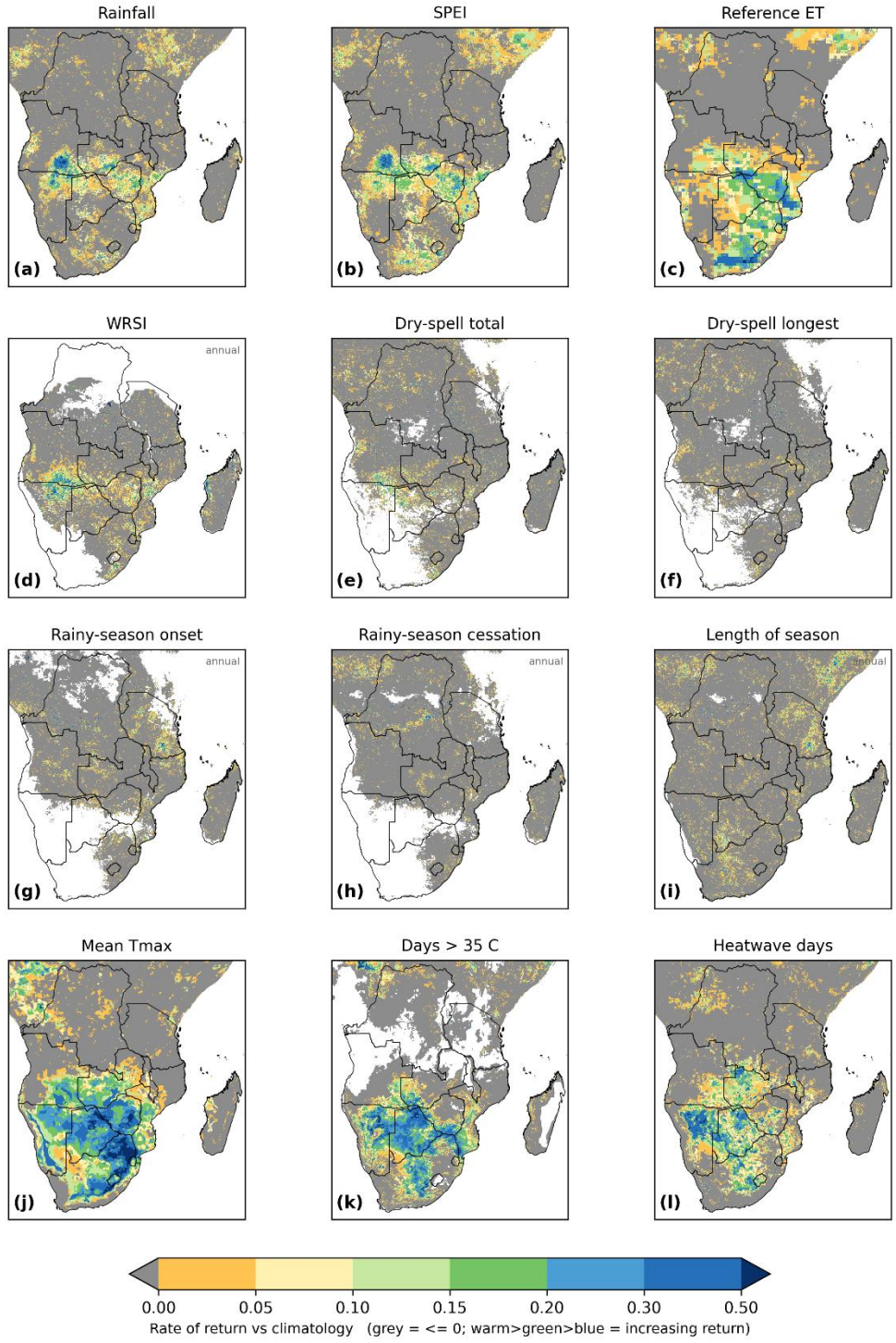

Fig. S9. Phase-specific rate of return for El Niño: a likelihood-based score expressed as an investment return relative to a 1/3 climatology (Hagedorn and Smith, 2009); grey marks no positive return, warm to green to blue an increasing one. Being a geometric-mean likelihood it is the most demanding of the four, so it turns positive only where the phase signal is both discriminating and well calibrated.

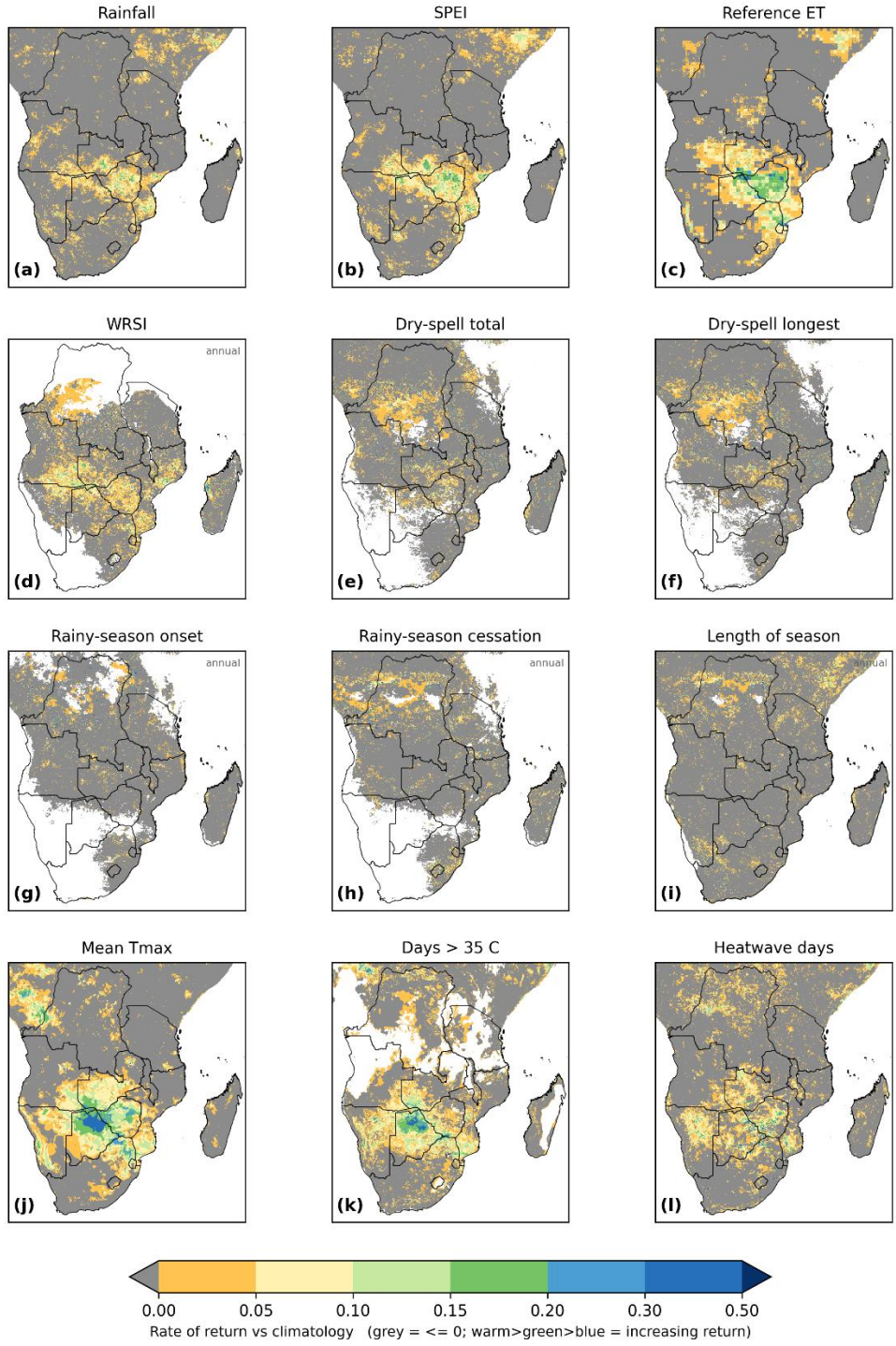

Fig. S10. Similar to Fig. S9, but for La Nina. Phase-specific rate of return for La Niña. Grey marks no positive return, warm to green to blue an increasing one.